



A framework for assessing tunnel drainage-induced impact on terrestrial vegetation



Cagri Gokdemir^a, Yi Rui^a, Yoram Rubin^b, Xiaojun Li^{a,*}

^a Department of Geotechnical Engineering, College of Civil Engineering, Tongji University, 1239 Siping Road, Shanghai 200092, China

^b Department of Civil and Environmental Engineering, University of California, Berkeley, CA 94720-1716, USA

ARTICLE INFO

Keywords:

Vulnerability assessment

Tunnel drainage

Numerical groundwater modeling

Mountain tunnel

ABSTRACT

The tunnel projects elevate the transport of large cities, but they also bring negative impacts on the terrestrial vegetation, particularly in mountainous rural areas. Aside from the immediate effects during construction, the tunnel drainage can have long-term effects on the terrestrial vegetation by depleting shallow groundwater resources adjacent to the tunnel. Previous research proposed a number of analytical and numerical methods for determining allowable tunnel drainage rates in order to keep terrestrial vegetation from wilting. These methods, however, only provide local estimates of drainage-induced drawdown and an approximate steady-state groundwater budget based on tunnel design parameters, ignoring soil water dynamics that have a direct influence on vegetation roots. As a result, we propose a comprehensive integral vulnerability assessment framework (IVAF) for assessing tunnel drainage's long-term regional impact on terrestrial vegetation. This framework couples a stochastic groundwater model, including tunnel parameters, with a topsoil model that includes soil–plant–atmosphere continuum (SPAC) components and creates regional vegetation vulnerability maps based on the vulnerability concept. It aims to provide a tool for tunneling experts by revealing the long-term tunnel drainage-induced changes between regional groundwater and soil water. The vulnerability assessment was applied to an example tunnel project in a moderately mountainous region. Vulnerability maps reveal the most likely influenced zones by tunnel drainage. The vulnerability index has been summarized via rooting depth segmentation, demonstrating the drawdown effect on topsoil. The assessment results show that IVAF is capable of establishing detailed groundwater and land cover connectivity on topsoil levels in poorly-sampled areas, as well as identifying potential vulnerability caused by tunnel drainage-induced drawdown.

1. Introduction

With increased economic development, there is a tendency to use underground space globally, particularly in emerging economies. Nowadays, underground space usage is dominantly needed for the highway and railway tunnels due to the demand for interconnecting growing urban regions. The majority of tunnels in mountainous areas were built due to encountered obstacles where groundwater levels are relatively higher than in low-relief terrain and are controlled by the topography (Condon and Maxwell, 2015; Gleeson and Manning, 2008). Tunnel construction in high- or moderate-relief mountain topography takes place inside the water-bearing ground, necessitating groundwater extraction via drainage throughout the tunnel's life span. However, groundwater extraction through tunnel drainage during the construction and maintenance period may result in a large drawdown and have

an irreversible environmental impact on terrain vegetation. From experience, drainage-induced drawdown may trigger ground settlement (Chu et al., 2022; Yoo et al., 2012; Zangerl et al., 2003), draining of springs (Gisbert et al., 2009; Guo et al., 2019; Wang et al., 2016), and soil water (Li et al., 2018). The tunnel drainage alters the natural state of the regional flow regime in the mountainous regions. Scheidler et al. (2019), drains the groundwater levels below base levels, and has a negative impact on the mountain streams (Vincenzi et al., 2014, 2009). In the long term, the persistence of terrain vegetation depends on the balance between the discharge from tunnel drainage and recharge from runoff and infiltration. When total groundwater discharge exceeds groundwater replenishment, soil water storage, which is necessary for terrain vegetation, depletes.

Drainage is an important component of tunnel design because it reduces the groundwater pressure on the tunnel lining. Sometimes, it is

* Corresponding author.

E-mail address: lixiaojun@tongji.edu.cn (X. Li).

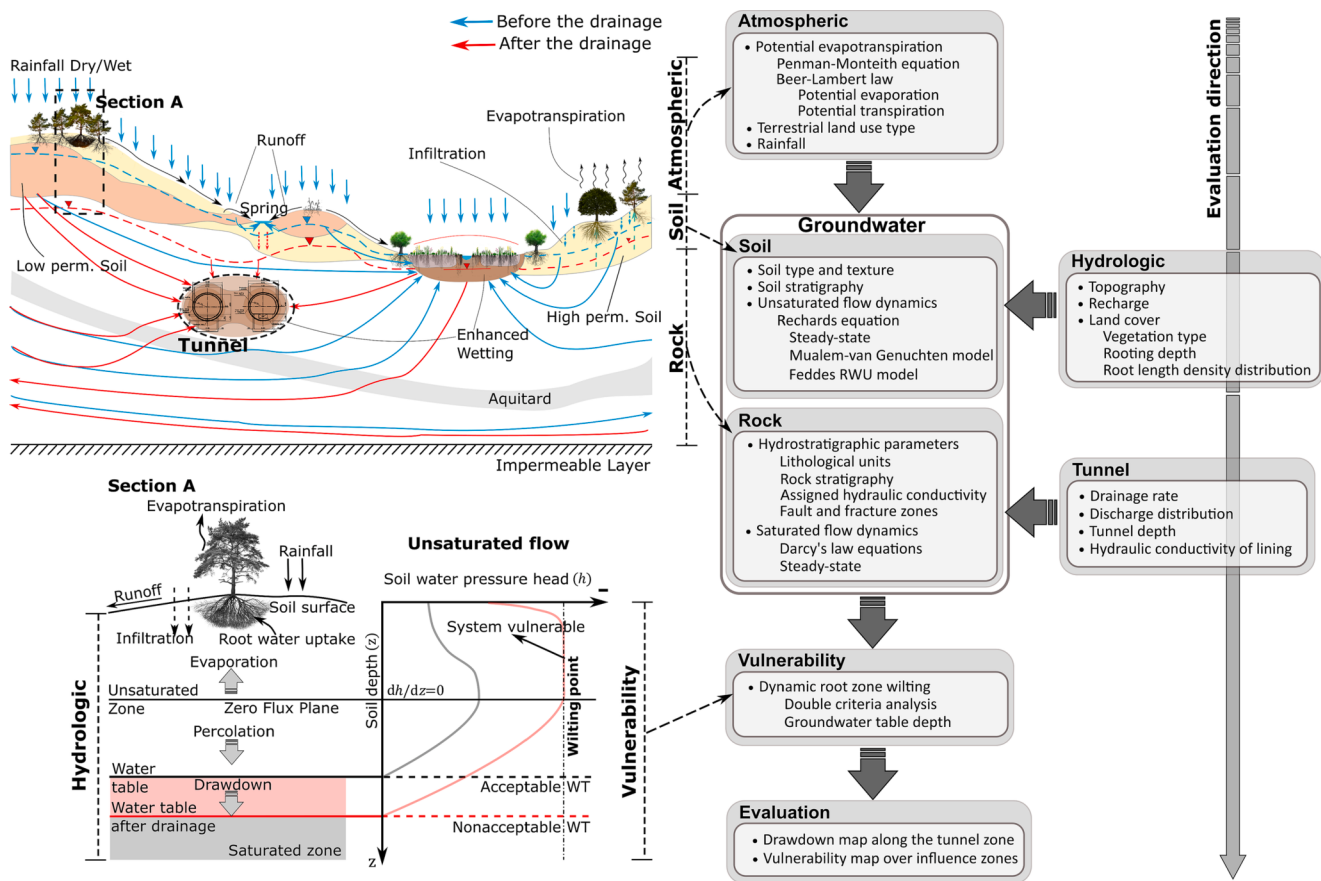


Fig. 1. The conceptual model for the assessment framework includes all the physical components of the tunnel drainage impact problem. Section A represents the topsoil profile influenced by changing groundwater table conditions.

preferable to cover surrounding groundwater rather than discharge it. However, high groundwater levels in mountainous areas necessitate controlled drainage. The lack of drainage may cause deformation and water outbursts in the tunnel (Zhao et al., 2013). Carefully regulated drainage may transfer the groundwater seepage and discharge the water, decreasing groundwater pressure on the tunnel by keeping the drawdown on an allowable level while avoiding the groundwater environment distress.

Due to the emphasis placed on maintaining the integrity of the infrastructure and protecting the environment, determining the allowable drainage rate is frequently used to limit tunnel water seepage (Cheng et al., 2014). Based on practical experience during the tunneling processes, some works considered permissible seepage via controlling tunnel drainage for mountainous ecology in terms of recreational areas and surface water resources (Liu et al., 2015). In addition, some numerical and analytical methods have been developed to quantify the seepage rate into tunnels in accordance with the on-site observations (Butscher, 2012; Cheng et al., 2019, 2014; El Tani, 2003; Farhadian and Nikvar-Hassani, 2019; Fernandez and Moon, 2010; Kolymbas and Wagner, 2007; Rasouli Maleki, 2018; Ribacchi et al., 2002; Su et al., 2017). Only Cheng et al. (2014; 2019) determined the limiting drainage rate using the ecological groundwater table, a concept that relies on the assumption of the maximum rooting depth of the vegetation in a mountainous region (Wan et al., 2005). With environmental concerns, the attention on limiting groundwater drainage has grown in the last decade. However, when it comes to water seepage, the definition of "allowable" is ambiguous and heavily reliant on practical experience. As a result, environmental control is typically accomplished through indirect means.

Limited studies evaluated the impact on vegetation by targeting the

magnitude of water-table drawdown induced by tunnel inflow based on the comparison between the drawdown and the deepest rooting depth (Cheng et al., 2019, 2014; Li et al., 2018). Even if the magnitude is only a few meters, vegetation species may change due to long-term drawdown (Jukaine et al., 1995; Cooper et al., 2006). Furthermore, some studies focusing on the water-table effect on terrain vegetation underscore soil water dynamics depending on the drawdown (Hosty and Mulqueen, 1996; Jin et al., 2007). The tunnel inflow reduces soil water content and alters plant water uptake patterns (Liu et al., 2019). Accordingly, Gokdemir et al. (2019) incorporated vulnerability criteria in the soil based on plant wilting caused by drainage-induced drawdown. Despite the fact that approaches to the tunnel seepage via rock and topsoil recharge are improving (Gokdemir et al., 2019, 2021; Sweetenham et al., 2017), the nexus between the drainage impact on vegetation and long-term tunnel drainage is unclear. Previously, an attempt was made to demonstrate briefly the change in drainage-induced drawdown depending on the tunnel diameter and depth from the land surface (Fernandez and Moon, 2010; Su et al., 2017). A study that connects tunnel design to the factors that limit the impact on vegetation, on the other hand, is lacking.

The tunnel inflow is influenced by two types of factors: 1) structural factors based on tunnel design parameters such as the tunnel length, diameter, depth from the land surface, and lining hydraulic conductivity, and 2) hydrologic factors such as atmospheric forcing, soil type and depth, land cover (e.g., vegetation type) and topography, bedrock type. Given that the majority of the deep tunnels reported in the literature are built beneath the mountain formations, the topographical controls on surface recharge also apply (Grinevskii, 2014; Yeh and Eltahir, 2005). The magnitude of tunnel seepage is determined by the complex interaction of structural and hydrologic factors. As a result, estimating allowable tunnel drainage based on vegetation resilience necessitates

taking into account the relationship between these factors. The vegetation and land surface processes such as runoff and evapotranspiration are represented by Soil-plant-atmosphere continuum (SPAC) perspective (Norman and Anderson, 2005). To model atmospheric effects on soil water and plant growth dynamics, the SPAC approach has been used in agricultural studies for crop modeling and water usage efficiency (Duan et al., 2019). Thus, we adopted the SPAC viewpoint to address the hydrologic factors in this work. Based on changes in hydraulic and structural factors, the study estimates the circular tunnel seepage. It proposes a comprehensive tool for assessing the impact of drainage on the safety of terrain vegetation.

In this study, we present the integral vulnerability assessment framework (IVAF) concept, with the goal of assessing tunnel drainage-induced impact on terrestrial vegetation based on ecological constraints on groundwater table depth.

2. Assessment framework

Based on the soil-plant-atmosphere continuum (SPAC), we propose an assessment framework for terrestrial vegetation. As a result, the framework connects atmospheric forcing with soil hydrology, as well as land cover parameters like terrestrial vegetation and plant physiology. The framework introduces groundwater dynamics in the rock environment and integrates tunnel with the SPAC components.

2.1. Conceptual model and framework

A conceptual model for the assessment framework is formulated to represent the impact of tunnel drainage on groundwater and on terrestrial vegetation (Fig. 1). Tunnel drainage, according to the model, lowers the regional groundwater table. It affects the amount of water that plants can access in the soil. Additionally, based on the tunnel's location, drainage alters the groundwater flow regime in the rock environment by diverting the flow direction. We concentrated on local soil water dynamics, which represent the hydrologic relationship between atmospheric factors and the groundwater table in addition to regional effects. The assessment framework analyses the water dynamics in the topsoil and root system to assess the state of the terrain vegetation.

By incorporating several theoretical notions into numerical models, the general assessment methodology is used to evaluate the drainage-induced impact according to vulnerability (See section 2.4.1). We combined a stochastic groundwater model with a topsoil model and extended the application over a tunnel region to conduct a vulnerability assessment spatially. Therefore, the assessment framework's methodology is called the integral vulnerability assessment method (IVAM). Section 2.2 provides additional information about the methodology.

2.1.1. Atmospheric forcing

The framework's atmospheric forcing function is to represent the atmosphere-soil interface in order to estimate soil water flux seeping into the soil. The water balance model is defined as follows:

$$P - ET = P - \varepsilon_c - \varepsilon_s - \tau = \begin{cases} 0 \\ \pm q_0 \end{cases} \quad (1)$$

where in equilibrium, the average precipitation, P [LT^{-1}], can be equal to the water amount lost from the average potential evapotranspiration, ET [LT^{-1}], including canopy evaporation, ε_c [LT^{-1}], soil evaporation, ε_s [LT^{-1}], and stomatal transpiration of the plants, τ [LT^{-1}]. We assumed that all of the intercepted rainfall evaporates from the vegetation canopy. As a result, canopy interception equals potential canopy evaporation. ET , thus, includes total evaporation, ε ($\varepsilon_c + \varepsilon_s$), and stomatal transpiration rate. Initial water flux, q_0 [LT^{-1}], percolates into the soil or evaporates from the soil in the absence of runoff. Here, ET is calculated using the crop coefficient approach (Allen et al., 1998):

$$ET = k_c ET_0 \quad (2)$$

where k_c is the crop coefficient [-] representing the terrestrial plant characteristics varying depending on soil water pressure head (see section 2.2.2), ET_0 represents the reference evapotranspiration [LT^{-1}] calculated from meteorological data using the Penman-Monteith equation (Monteith, 1981; Monteith and Unsworth, 2013). k_c value is assumed to be constant in the framework for the fully-grown plants.

Based on Beer's Law application on plant canopy transmittance (Gower et al., 1999), the partitioning between potential transpiration and total evaporation fluxes has been estimated as follows:

$$\tau = ET \bullet SCF \quad (3)$$

$$\varepsilon = ET \bullet (1 - SCF) \quad (4)$$

SCF is the soil cover fraction for the chosen location represented as follows:

$$SCF = 1 - \exp(-k \bullet LAI) \quad (5)$$

where k is the light extinction coefficient by plant canopy [-], and LAI is the leaf area index [LL^{-1}]. Interception, I [LT^{-1}], is also taken into account using the LAI parameter, including the following equation:

$$I = a \bullet LAI \left(1 - \frac{1}{1 + \frac{SCF \bullet P}{a \bullet LAI}} \right) \quad (6)$$

Interception is estimated as a function of precipitation, SCF , LAI , and a is a constant used to calibrate the parameters according to the field precipitation data. ε_s ($\varepsilon_s = I$) can be calculated using Eq.6 to estimate the fraction in total evaporation. The selected values for atmospheric forcing are listed in the assessment application section.

2.1.2. Groundwater

The groundwater includes two components interconnected in the framework: soil water and saturated water within the rock mass, which are separated for computational and parameterization reasons. The main focus of the assessment framework on groundwater dynamics is the unsaturated-saturated soil interface, which includes groundwater-vadose zone interaction as a hydrologic phenomenon. The topsoil model represents the transition from saturated to unsaturated soil, including atmospheric forcing and plant rooting zone. Furthermore, the groundwater drawdown influences the extent of the unsaturated zone defined by a separate system for groundwater flow in the rock zone. Therefore, the framework treats topsoil and groundwater in the rock zone as discrete but interconnected systems. Section 2.2 describes the numerical representation and parameterization in detail.

2.1.2.1. Unsaturated flow in soil. The soil water is defined as the sum of the moisture content and the saturated portion of the topsoil overlying rock layer (Fig. 1). For vertical flow, the modified Richards equation represents the dynamic between the saturated and unsaturated portions of the topsoil:

$$\frac{\partial \theta(h)}{\partial t} = \frac{\partial}{\partial z} \left[K(h) \left(\frac{dh}{dz} + 1 \right) \right] - S(h, z, \tau), \quad (7)$$

where $\theta(h)$ stands for volumetric soil water content [$\text{L}^3 \text{L}^{-3}$]; t is time [T]; h represents the soil water pressure head [L]; z is the spatial coordinate [L] in vertical plain; $K(h)$ is unsaturated soil hydraulic conductivity as a function of pressure and vertical distance [LT^{-1}]; and $S(h, z, \tau)$ is the sink term for the root water uptake [$\text{L}^3 \text{L}^{-3} \text{T}^{-1}$]. Depending on the soil water pressure head, Eq. (7) can switch between saturated and unsaturated conditions. Richards equation exhibits non-linear behavior under unsaturated conditions and linear behavior under saturated conditions. Boundary conditions and numerical details are presented in section 2.2.

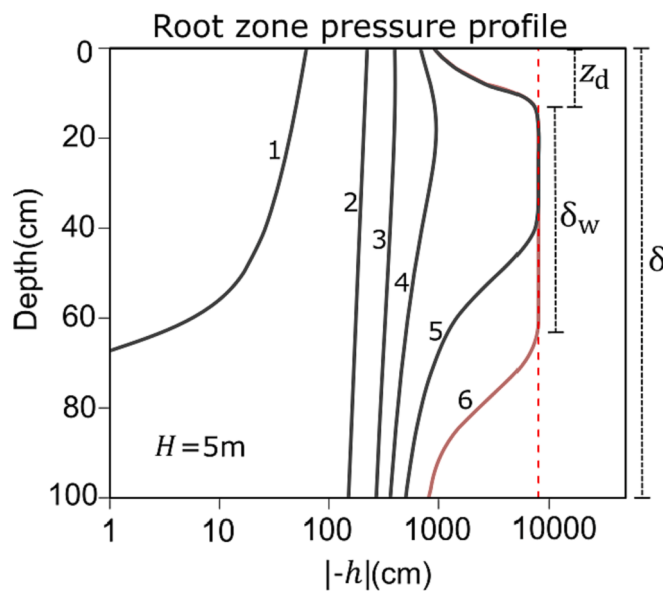


Fig. 2. Graphical demonstration of root-zone wilting and parameterization of vulnerability condition in homogeneous low permeability topsoil. The numbered curves represent soil water pressure head under equilibrium for different atmospheric forcing over groundwater level of 5 m. The vertical discontinuous line in red represents the wilting point ($h_w = -8000$ cm). In the soil profile, rooting depth (δ) is assumed to be 100 cm. The crimson curve (number 6) demonstrates the condition where vulnerability is satisfied, specifying wilting depth (δ_w). (For interpretation of the references to color in this figure legend, the reader is referred to the web version of this article.)

2.1.2.2. Saturated flow in a rock environment. The steady-state groundwater flow of an incompressible fluid at constant density in a continuous porous rock body is modeled based on Darcy's law for the three-dimensional domain:

$$\nabla \bullet (K_s \nabla H) + q_a = 0 \quad (8)$$

where H is hydraulic head [L]; q_a is the actual volumetric water flux into the rock mass seeping from the topsoil [$L^3 L^{-3} T^{-1}$]; $\nabla \bullet = \frac{\partial}{\partial x} + \frac{\partial}{\partial y} + \frac{\partial}{\partial z}$ represents the divergence operator; $\nabla = \left(\frac{\partial}{\partial x}, \frac{\partial}{\partial y}, \frac{\partial}{\partial z} \right)^T$ is the gradient for the scalar values; and K_s is the saturated hydraulic conductivity of a rock type [LT^{-1}]. The saturated groundwater flow is modeled separately from the soil layer. Recharge flux, on the other hand, is included as the source term q_a and represents the volume of water per aquifer area (LT^{-1}) infiltrated from the topsoil.

2.1.3. Vegetation system

The vegetation structure is included in the framework as a root system in the topsoil. The assumptions have been made based on the dominant vegetation type overlaying the land surface. Thus, the rooting system is the inherent component of the topsoil and has a direct influence on the soil water pressure head. A fully grown vegetation rooting system is designed with a root density distribution function (Dos Santos et al., 2017):

$$R(z_r) = \frac{b^2 R_{avg}}{b + e^{-b} - 1} (1 - z_r) e^{-bz_r} (b > 0). \quad (9)$$

where $R(z_r)$ is root length per unit soil volume [LL^{-3}] as a function of relative rooting depth z_r [LL^{-1}], which is the ratio of the vertical coordinate in the soil column against rooting depth ($= z/\delta$); R_{avg} represents root length density value [LL^{-3}]; and b is the root shape-factor [-] depending on the vegetation type. $R(z_r)$ spatially controls root water uptake along the rooting depth and is integrated with sink term $S(h, z, \tau)$ can be written as:

$$S(h, z, \tau) = \mu(h) S_p(h, z, \tau) \quad (10)$$

where $S_p(h, z, \tau)$ is the normalized potential root water uptake rate [T^{-1}]; $\mu(h)$ is water stress response function ($0 \leq \mu(h) \leq 1$) applied based on Feddes et al. (1974, 1978). Normalized $S_p(h, z, \tau)$ is

$$S_p(h, z, \tau) = \frac{R(z_r)}{\int_{z_r^{\max}}^{z_r^{\max}} R(z_r) dz_r} \tau \quad (11)$$

The denominator in Eq. (11) ensures unity over the maximum relative rooting depth (z_r^{\max}). Integrating Eq. (10) over rooting depth yields the actual transpiration flux (τ_a).

$$\tau_a = \int_0^{\delta_w} S(h, z, \tau) d\delta \quad (12)$$

given the above equations, τ_a is regulated by $\mu(h)$, where root water uptake approaches zero under saturation and wilting conditions. Conversely, when $\mu(h)$ value becomes 1, the water uptake rate reaches its maximum (Feddes et al., 2001, 1978). In the framework, vegetation is assumed to be ceased to exist only in wilting conditions.

2.1.4. Vulnerability concept

The ecological groundwater table concept has been introduced based on field surveys from a mountainous tunnel site indicating groundwater drawdown exceeding the largest rooting depth considered harmful to terrestrial vegetation (Wan et al., 2005). Thus, the drainage limitation has been proposed to maintain the groundwater table at a certain level where terrestrial vegetation remains intact, known as the ecological groundwater table. Accordingly, previous studies on the impact of tunnel drainage focused on the groundwater table as an indicator parameter (Cheng et al., 2019; Li et al., 2018). The survival of terrestrial vegetation in the mountainous region, however, is controlled by soil water content as a function of h , which has a non-linear relationship with groundwater table alterations (See Appendix A). Therefore, in the framework, we considered the vulnerability concept, highlighting the vulnerability condition in which h reduces to the permanent wilting point, h_w (Gokdemir et al., 2019).

The vulnerability concept proposes dynamic root-zone wilting, including the double vulnerability criteria in a rooting zone. The dynamic root-zone wilting requires the detailed soil water pressure head analysis on the topsoil associated with the wilting depth (δ_w) demonstrated in Fig. 2. We are looking for two criteria satisfying the vulnerability condition: (1) if h falls below the permanent wilting point ($h = h_w$ at z); (2) if h_w occupies at least 50 % of the total rooting depth ($\delta_w/\delta \geq 0.5$).

To explain vulnerability analysis for the framework, the soil pressure head profile as a function of the soil depth on a semi-logarithmic scale is shown. In Fig. 2, z_d is the wetting front formed close to the soil surface as a result of rapid infiltration, which is mostly visible during the drying conditions. δ_w is considered after subtracting z_d from the rooting depth, selected as 100 cm in this example. The topsoil pressure profiles shown in Fig. 2 are estimated over the groundwater table at a depth of 5 m. Profiles in equilibrium numbered from 1 to 4 demonstrate non-vulnerable conditions, whereas profile 5 meets only the first criterion, and profile 6 meets both vulnerability criteria with $>50\delta_w$ cm. Profile 5 reaches vulnerability, but the plant survives. Differently, profile 6 depicts a situation in which the plant ceases to exist. Pressure profile analysis, in addition to testing vulnerability criteria, provides an update for the groundwater table, as seen in profile 1, where the saturation level rises to 75 cm depth under equilibrium.

2.2. Assessment methodology

The Integral Vulnerability Assessment Method (IVAM) is composed

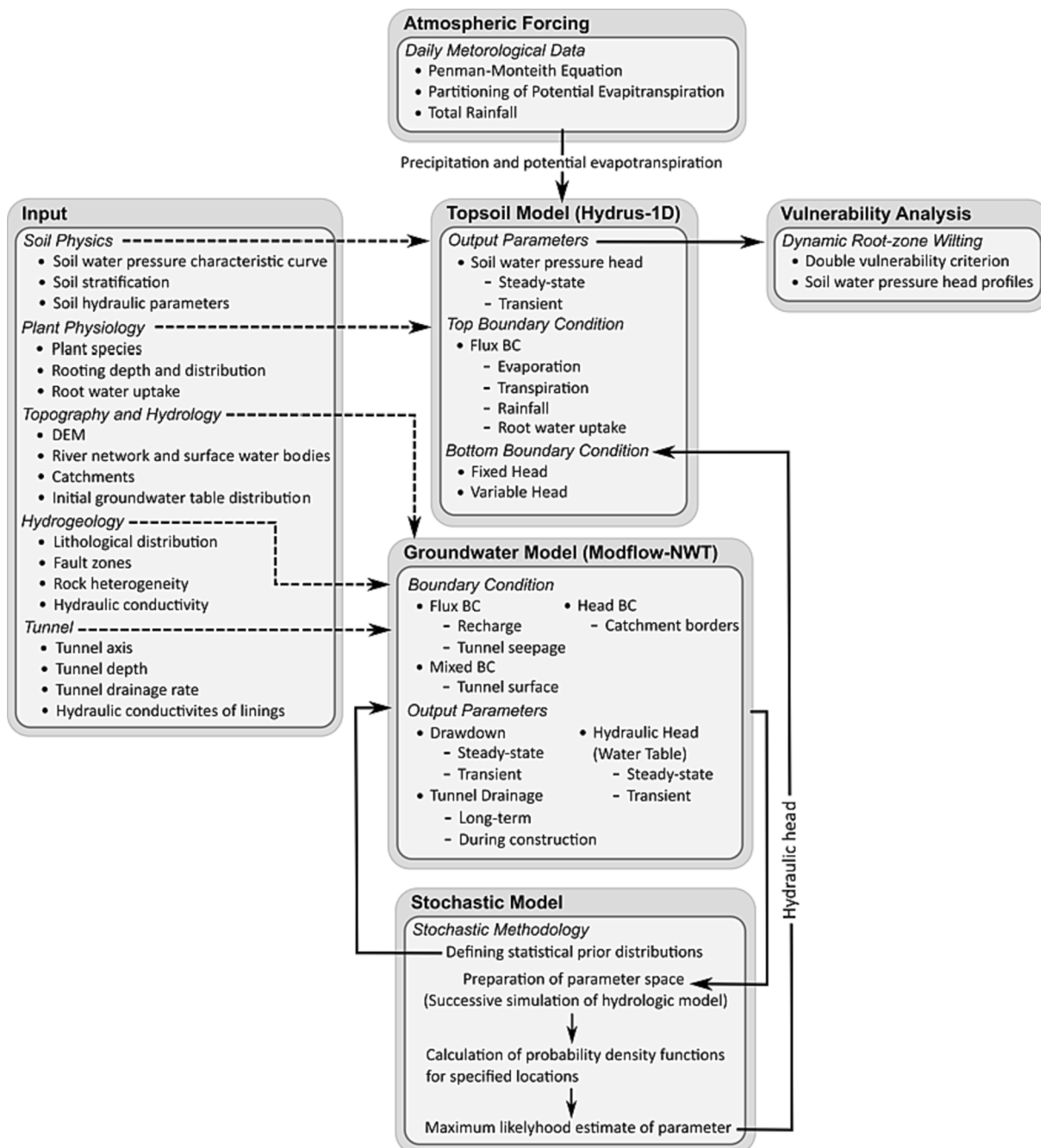


Fig. 3. Schematic outline of integral vulnerability assessment method (IVAM) for the tunnel drainage-induced impact assessment.

of coupled numerical topsoil model and a stochastic groundwater model (Fig. 3), including the factors representing SPAC. The method is intended to generate a spatial regional impact assessment map along the tunnel where IVAM is used. Based on the profile analysis presented in section 2.1.4, the vulnerability condition is tested at each point along the tunnel region (Fig. 2). The vulnerability index (h/h_w) at depth z_r is reported as a result of regional analysis, and vulnerability maps are summarized as percentage changes for relative rooting depth. Vulnerability index (V_{in}) ranges between 1 and 0, with 1 representing a wilting condition. At the same time, any value <1 approximates the wilting point.

2.2.1. Stochastic groundwater model

A stochastic estimate of drawdown was used, which combined a numerical groundwater model with Bayesian statistics conditioned on

normalized tunnel inflow. As a result, the stochastic groundwater model is defined as a probabilistic model that employs a numerical model to physically represent groundwater flow dynamics (Gokdemir et al., 2022; Li et al., 2018). The probabilistic model is described below;

$$P(d(x) \in \mathcal{D} | e_k) = \sum_{j=1}^M \{P(d(x) \in \mathcal{D}) | e_k, H_j\} P(H_j | e_k), \quad (13)$$

where P stands for probability, $d(x)$ is the drawdown estimate [L] modeled as a random variable at location x . The left-hand side of the equation represents the probability mass function conditioned on error interval, $e_k, k = 1, \dots, K$, which is the difference between simulated and actual normalized groundwater inflow [$L^{3-1}T^{-1}$] can be expressed as $|q_s - q_{in}|$. The right-hand side is divided into M number of hypercubes as a subset of H_j representing the j^{th} division of parameter space θ used for

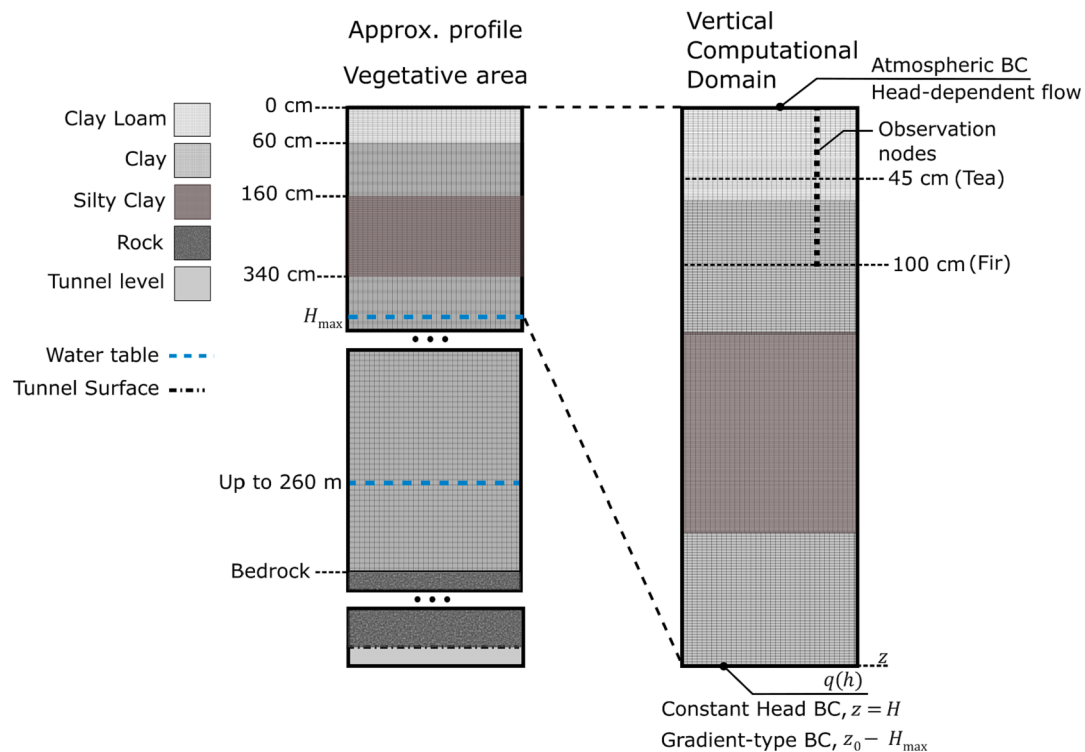


Fig. 4. Representative schema of 1-D topsoil model with approximate profile and the computational domain used in the assessment method.

the Monte Carlo integration; $P(H_j|e_k)$ is hypercube probability conditional to e_k . \mathcal{D} represents the entire drawdown dataset [L] for a specific location. Using Eq. (13), the most likely drawdown can be estimated for any point in the tunnel region.

To solve Eq. (8), the steady-state groundwater flow field impacted by tunnel drainage was simulated using Modflow-NWT, a cell-centered finite-difference code (Harbaugh, Arlen and Harbaugh, 2005). θ was created in the form of ex-situ priors as a vector for hydraulic conductivity information per rock type and recharge (Li et al., 2018). For the series of numerical groundwater flow simulations, the input parameters were sampled from the prior distribution. Accordingly, simulation results were used to build \mathcal{D} and the sets of e_k to employ in Eq. (13).

The numerical model was discretized using variable grid refinement, with the fineness of the grid increasing towards the tunnel location from the outer edges of the model domain. The primary model domain represents the tunnel area, which is our zone of interest, and the overall model resolves the regional groundwater system. Three types of boundary conditions were employed: a perimeter and two internal boundary conditions. The head boundary condition was applied to the defined boundaries of the multi-catchment area, which is expressed as

$$H|_{\Gamma_1} = H_0(x) \quad x \in \Gamma_1 \quad (14)$$

where H_0 denotes the specified water table level and x represents spatial dimensions on boundary Γ_1 . Flow boundary condition was applied to represent recharge from the soil over the model domain

$$K_s \nabla H|_{\Gamma_2} = q_a(x) \quad x \in \Gamma_2 \quad (15)$$

The top boundary of the discretized model domain is Γ_2 , representing the face of bedrock. In the groundwater model, the tunnel is treated as a drain represented by mixed boundary condition, which is summarized as

$$q_{in}(x) = \begin{cases} C(H|_{\Gamma_3} - H_{ref}|_{\Gamma_3})H > H_{ref} & x \in \Gamma_3 \\ 0H \leq H_{ref} & \end{cases} \quad (16)$$

where q_{in} is the inflow through the lining that serves the tunnel surface as the boundary Γ_3 . C is the boundary conductance [L^2/T] referring to $K_L A/L$, where K_L is the equivalent hydraulic conductivity [LT^{-1}] of shotcrete and lining, A is the total area [L^2] through which water flows. L is the total thickness of the lining and shotcrete layers [L]. H drops to reference hydraulic head, H_{ref} , over the length L , where H_{ref} is set to be zero, because the groundwater pressure on the tunnel surface reduces nearly to zero due to drainage.

2.2.2. Topsoil model

The topsoil model reveals the soil water pressure head distribution along the vertical soil column. Topsoil simulations were conducted using the parallel columns approach, assuming decoupled soil columns with different properties per land cover (Rubin and Or, 1993). The steady-state topsoil model was simulated using Hydrus-1D, a one-dimensional finite-element code to solve Eq. (7) (Šimunek et al., 2013). In Eq. (7), the relationship between $K(h)$ and $\theta(h)$ was modeled using the Mualem-van Genuchten hydraulic model under hysteretic conditions with an air entry (van Genuchten, 1980). The formulation of soil parameters and application of the hydraulic model is summarized in Gokdemir et al. (2019, 2021).

Three boundary conditions are applied to a single soil column as a head-dependent flow boundary condition on the soil surface;

$$\left. K(h) \left(\frac{dh}{dz} + 1 \right) \right|_{z=z_0} = |q_0| h_{min} < h < 0 \quad (17)$$

Head boundary condition

$$h|_{z=H} = 0 \quad (18)$$

and gradient-type (Free drainage) boundary condition as the lower boundary of the soil column;

$$-K(h)|_{z < H_{max}} = q(h)h < 0 \quad (19)$$

In Eq. (17), z_0 is the soil surface elevation, and h_{min} is the allowable minimum pressure head at the soil surface. The value of q_0 is determined

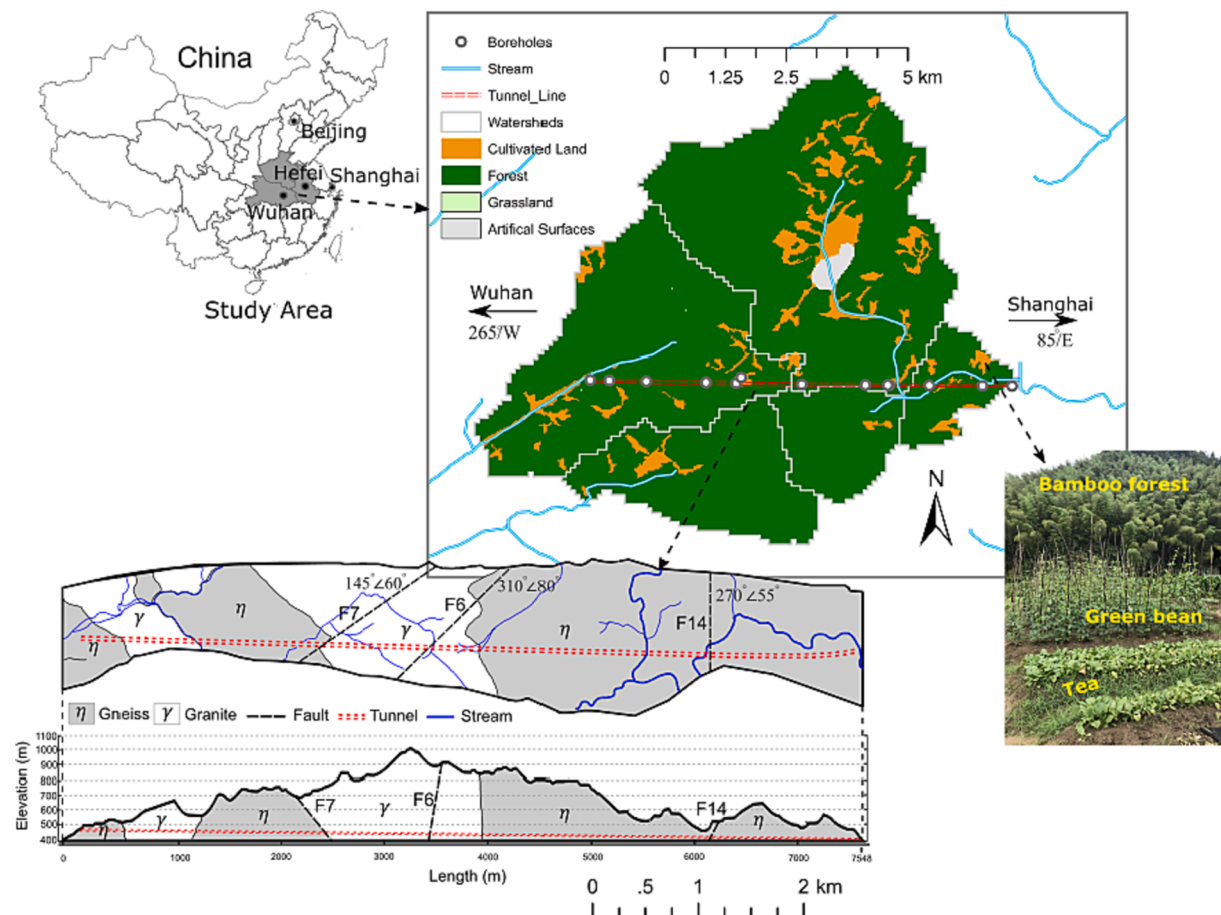


Fig. 5. Geographic information of the area of interest, including the tunneling site: The catchment areas corresponding to the tunnel line and overlying land cover with 30 m resolution (Chen et al., 2017) are mapped; distribution of rock from the borehole analysis is also demonstrated with terrain elevation.

by the imposed atmospheric conditions (See Eq. (1)). Eq. (18) represents the water table level predicted by the stochastic groundwater model ($H = H_0 - d(x)$), which is used as the initial boundary condition for the topsoil model. Eq. (19) depicts the deep groundwater table condition, where the water table remains far below the rooting zone. When H exceeds the maximum water table, H_{\max} , the outflow from the vertical computational domain, $q(h)$, is calculated based on local h (Fig. 4). While H_{\max} varies due to the location, the depth-to-water table (DWT) remains constant according to $(z_0 - H_{\max})$.

3. Assessment application

3.1. Case study

The study area is a part of a highway project connecting provinces of Hubei and Anhui, with the tunnel being built in Yuexi County in Anhui Province, China. The study area consists of five catchments dominated by seasonal streams and intersecting tunnel lines (Fig. 4). The construction is conducted on the highest ground of a middle-low mountainous area with an average hillslope of 30°–45°. The ground elevation varies between 300.0 and 1300.0 m over whole catchment areas. The topsoil comprises soft soil types layered as silt, silty clay, sandy clay, and clay loam textures, with depths ranging from 10 to 15 m. Site surveys from the boreholes indicate that the tunnel line crosses moderately weathered granite and gneiss rock bodies and corresponds to three fault zones marked as F7 (145°±60°), F6 (310°±80°), and F14 (270°±55°) in Fig. 5 (Chen et al., 2016; Li et al., 2016). The tunnel zone encompasses seasonal streams that vary in response to atmospheric precipitation; thus, water flow is primarily topography-driven. The area is typical of a

humid region with an average precipitation of 1452 mm/year, where groundwater levels are influenced by seasonal atmospheric conditions and topography (Schaller and Fan, 2009).

The Mingtang tunnel case study is a typical example of the impact of a large tunnel construction (7.6 km) on a rural area where information is limited and difficult to obtain. With scarce data, this case study provides the opportunity to assess the impact of tunnel drainage on mountainous areas. Borehole readings from 12 different locations along the tunnel axis are the only available data in the project. The study area is an altered zone as a result of early 1980s reforestation to a high-density coniferous forest dominated by Chinese fir (*Cunninghamia lanceolate*) with occasional distribution Chinese spruce (*Picea asperata*). The land cover of the tunnel area comprises sparse agricultural fields of various products, relatively large bamboo (*Phyllostachys pubescens*) forests, and limited grassland (Fig. 5). In the northern part of the designated region, where farmlands are located, the density of cultivated land increases. The agricultural land is dominated by paddy and tea fields (*Camellia sinensis*). The tunnel impact assessment has been applied to multiple catchment areas with defined land cover properties.

3.2. Integration and parameter values

The parameters of IVAF were chosen based on the interfaces in the SPAC and tunnel system, representing atmosphere-plant, atmosphere-soil, soil-rock, and rock-tunnel system interfaces. The transaction between interfaces results a weak integration of different models. The methodology is fully physical-based and is built around stochastic groundwater and topsoil models. The relationship between soil-plant-atmosphere and groundwater table interfaces is represented in the

Table 1

The summary of Integral Vulnerability Assessment Framework (IVAF) parameter values.

Integral Vulnerability Assessment Framework Parameters*								
Time step	Lower BC	Upper BC	Domain	Node spacing (cm) ^a	Run Length (yr) ^b	$\delta(\text{cm})^c$	$R_{\text{avg}}(\text{cm cm}^{-3})^d$	
Design parameters and boundary conditions for topsoil								
Topsoil (Hydrus 1-D)	Daily	Head (DWT \leq 30 m, Eq. (18))	Head-dependent gradient-type (DWT $>$ 30 m, Eq. (19))	1-D vertical soil column (Eq. (17))	0.001–25	8 <	100 (Fir)	1.0
							45 (Tea)	
Soil Type	Depth (cm)	$\theta_i(\text{cm}^3 \text{cm}^{-3})$	$\theta_s^w(\text{cm}^3 \text{cm}^{-3})$	$\theta_d^d(\text{cm}^3 \text{cm}^{-3})$	$\alpha_w(\text{cm}^{-1})^f$	$\alpha_d(\text{cm}^{-1})^f$	$n(-)$	$K_s(\text{m/s})$
Layered Soil hydraulic parameters								
Clay-Loam ^e	0 – 60	0.095	0.370	0.410	0.043	0.019	1.31	7.222E-07
Clay ^e	60 – 160	0.068	0.340	0.380	0.018	0.008	1.09	5.556E-07
Silty-Clay ^e	160 – 340	0.070	0.324	0.360	0.011	0.005	1.09	5.556E-08
Clay ^e	340 - profile depth	0.068	0.340	0.380	0.018	0.008	1.09	5.556E-07
	Time step	Boundary Conditions			Domain	Node spacing (m)^g	Simulation Length	Total simulation subsets
Design parameters and boundary conditions for stochastic groundwater model								
Stochastic groundwater model (Modflow-NWT 3-D)	Steady-state	Head (Eq. (14))	Flow (Eq. (15))	Mixed (Eq. (16))	3-D regional model	0.2–373.5	Single stress period	134
Material Type	Thickness (m)	Anisotropy	Porosity	Tunnel depth (m)	$K_s(\text{m/s})$		Recharge (m³d⁻¹)^h	
Hydraulic parameters								
Gneiss ⁱ	Along the domain	1.00	0.30	388–450	4.540E-05	5.043E-07	–	–
Granite ⁱ					1.120E-05	1.855E-07	–	–
Fault core ^j					4.600E-10	3.355E-04	–	–
Fault Damage zone ^j					2.754E-05	1.110E-02	–	–
Quaternary layer	50.00				2.71	3.30	30460.40	91381.30
Tunnel lining	0.35				3.819E-05		3069.40	5179.40
Shotcrete	0.10				4.244E-06			
Plant type	P (mm)^k	I (mm)^k	r(mm)^k	$\varepsilon(\text{mm})^k$	LAI (-)^l	SCF (-)^m	$k_c(-)$	$b(-)$
Atmospheric - Vegetation system parameters								
Chinese fir	1452.20	544.40	911.10	78.35	5.07	0.92	1.00	2.00
Tea plant		482.00	861.20	128.34	4.09	0.87		4.00

a: Variable discretization has been used with small mesh sizes in rooting zone and the proximity of water table.

b: Simulation lengths have been extended to reach equilibrium condition in given boundary conditions.

c: Average value for Chines fir is from Chen et al. (2013) and Gokdemir et al. (2019), tea plant is from Niranjana and Viswanath (2008).

d: From previously published distribution parameters from de Jong van Lier et al. (2006).

e: Class average values for van Genuchten model (1980) from Carsel and Parrish (1988).

f: The values are taken from the hysteresis experiments of Likos et al. (2014).

g: Variable grid refinement has been used (See Gokdemir et al. (2022)).

h: The recharge is annual aggregate value of water flux into the Quaternary layer (q_a) and inflow into the tunnel lining over the tunnel length (q_{in}).

i: The range of effective hydraulic conductivities for both rock types are selected from the assimilated ex-situ data presented by Li et al. (2018) based on site similarity perspective.

j: Values for fault core and damage zone include faults corresponding to both Gneiss and Granite rock types.

k: Annual values.

l: LAI is adopted for a converted high-density Chinese Fir forest (Farooq et al., 2020), and mature tea plantation (Rajapakse et al., 2002).

m: Standard value of 0.5 is used for the light extinction coefficient (k) by plant canopy.*Vulnerability analysis is based on h^* at -0.49 MPa (-5000 cm) and h_w at -79 MPa (-8000 cm) for each soil layer type. The calibrated value of a in Eq. (6) is calculated as 0.463.**Table 2**

Summary statistics of error intervals based on stochastic model outcomes. Intervals are reported as the minimum and maximum values with mean, standard deviation, variations, and subset sample size.

e_k interval	Min.	Max.	Mean.	Std.dev	Var.	n
<0.25	0.021	0.248	0.129	0.197	0.006	25
0.25–1.00	0.252	0.987	0.526	0.078	0.039	59
1.00<	1.048	26.84	10.394	0.076	89.892	50

topsoil model, whereas the stochastic groundwater model simulates the deeper groundwater and tunnel interaction.

The stochastic model includes 134 independent simulations of

groundwater flow for recharge values ranging from 6×10^{-4} and $18 \times 10^{-4} \text{ m s}^{-1}$ with the hydraulic conductivity range shown in Table 1. The simulation outcomes are used to populate the independent hypercube probability, $P(H_j)$, which is then conditioned on e_k to produce $P(H_j|e_k)$. From the left-hand side of Eq. (13), the subset of \mathcal{D} is divided into e_k intervals selected to have a reasonable subset size for the stochastic model (Table 2). For each location, a posterior drawdown distribution in Gaussian probability density function (PDF) format is created. Each PDF is used to estimate the mean, μ_x , which represents the most likely drawdown, and the standard deviation, σ_x , for uncertainty.

Topsoil simulations run over land cover data using parallel column approach (See section 2.2.2). Parameters and boundary conditions are therefore assigned per Chinese fir and tea plant location based on the

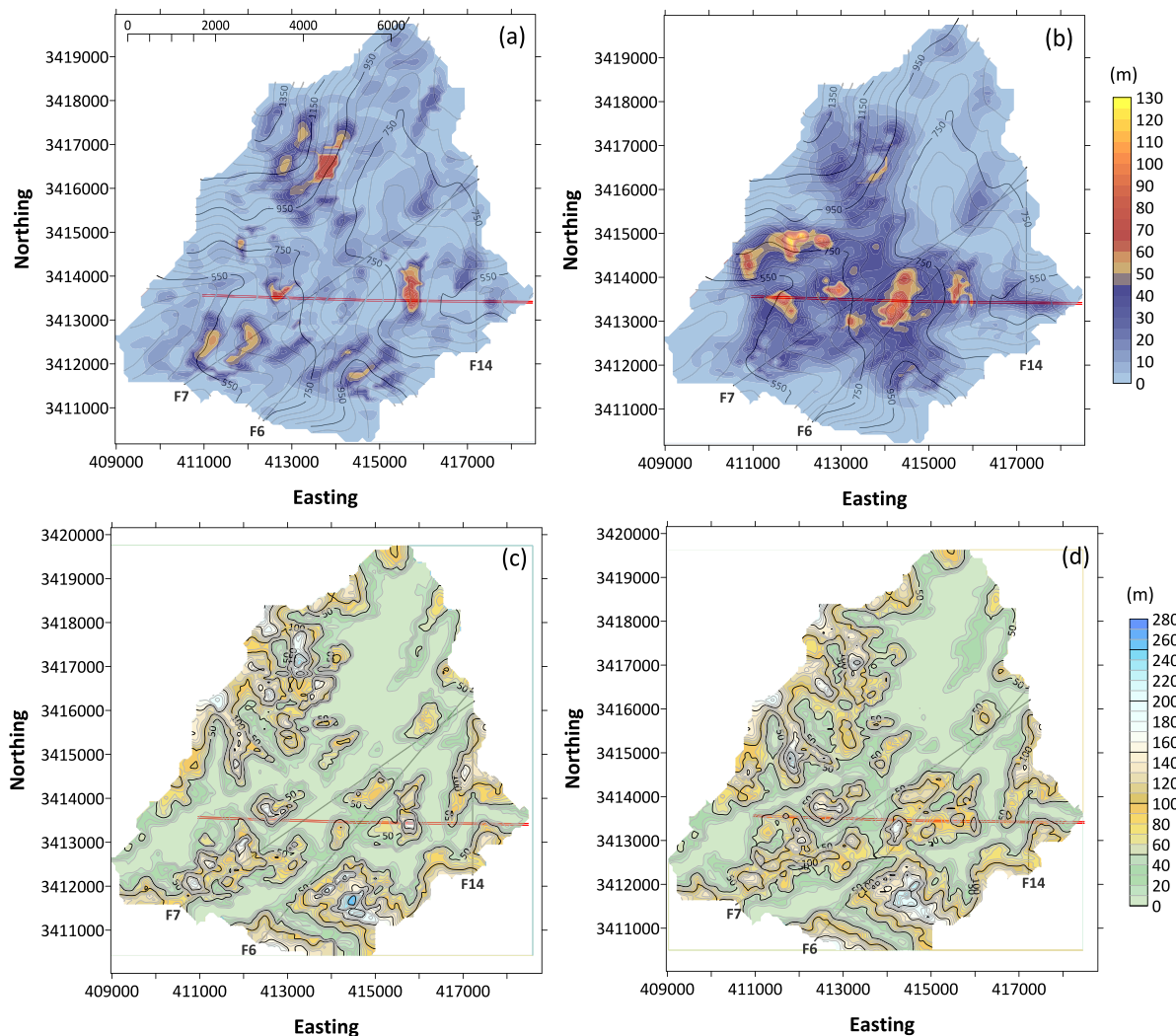


Fig. 6. Stochastic groundwater model outcomes as (a) drawdown and (c) depth-to-water table estimates. Uncertainty in standard deviation has also been presented for (b) drawdown and (d) depth-to-water table. Drawdown distributions are overlaid on the initial water table depicted as the gray contour lines.

associated land type and layered soil types (Table 1). The resolution for each representative soil column is averaged over the land cover to 90 m (30 m cell). The topsoil simulation run length is extended until the soil column reaches the equilibrium under given boundary conditions, approximating steady-state solution for Eq. (7). The simulation run time is limited to 8 years. The locations where the groundwater table is deep enough ($DWT > 30$ m) are run by switching gradient-type lower boundary condition. For computational purposes, the horizontal computational domain of the tunnel region is segmented based on DWT distribution (See Appendix B). Topsoil simulations are considered in the range of $0 \leq \mu_x \leq \mu_x + \sigma_x$ from the stochastic model, reflecting the drawdown uncertainty over the topsoil. Vulnerability analysis is performed separately for μ_x and σ_x estimates, with the difference revealing vulnerability uncertainty.

4. Results

4.1. Stochastic modeling of tunnel drainage-induced drawdown

The stochastic simulation results are presented in Fig. 6a and 6c as mean drawdown, and depth-to-water table map predictions, respectively, and σ_x -based maps are shown in Fig. 6b and 6d. The drawdown information (μ_x , σ_x) for each location on the map was estimated using PDFs generated from parameter combinations tabulated in Table 1 and

populated from the subsets of $e_k < 0.25$, summarized in Table 2.

Outcomes in Fig. 6a suggest that the average predicted drawdown for the entire region is 10.73 m, with a maximum value of 100.45 m. Approximately 72 % of the regional area has a drawdown value less than the regional average, and 2 % occupies a drawdown area deeper than 50 m, primarily in high-water table zones and the tunnel proximity. Fig. 6b depicts a drawdown distribution with an average of 25.5 m and maxima of 126.6 m, displaying a higher trend than Fig. 6a. By planar area, 53 % of the region is shallower, while the remaining 25 % is deeper than the average drawdown, which is mostly concentrated around the tunnel line. The vertical difference between the ground elevation and the water table after the drawdown is used to generate DWT maps. Unlike drawdown maps, the maximum DWT based on μ_x (260.47 m) does not differ significantly from the one shown in Fig. 6d (256 m). However, in σ_x -based DWT map, where most of the distinction clusters over the tunnel area, the shallow water zone (<10 m) decreases by 7 %,

Fig. 7 shows the tunnel drainage impact on the water table as a function of $2\sigma_x$ interval between predicted upper and lower bands. The portion from the mean estimate to the upper band demonstrates low-influence zone (light gray area) on the water table, while the lower band represents the high-influence zone (dark gray area). The majority of the upper band water table follows the natural water table levels along the tunnel axis, with the exception of the location between 4565 m and 4974 m from the western entrance (Blue area), where 69.3 m of

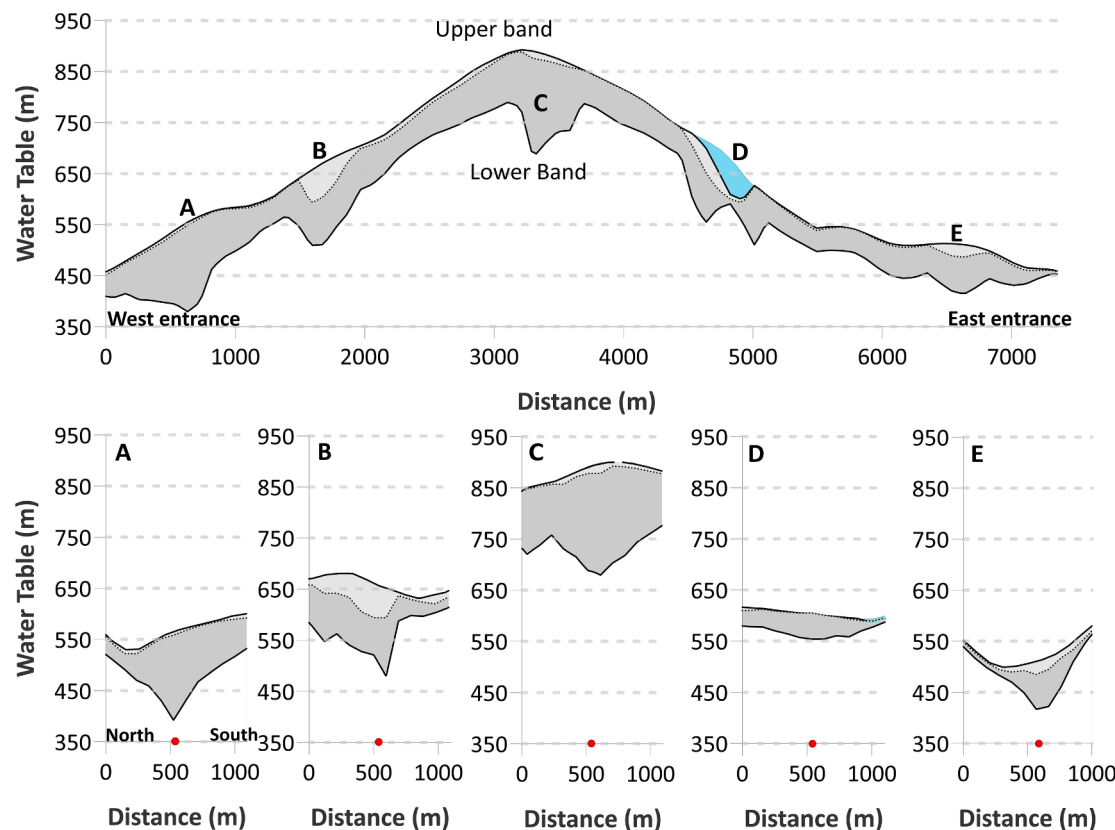


Fig. 7. The cross-sectional profile of the water table range according to $2\sigma_x$ interval representing >90 % of the likely hood from the mean water table (discontinuous line). The upper and lower bands are demonstrated based on $\mu_x \pm 2\sigma_x$ for each drawdown estimate. Dark and light gray areas represent the high-influence and low-influence zones, respectively. The blue area highlights the difference between $2\sigma_x$ range and the natural water table level. Upper figure demonstrates the cross-sectional profile on the tunnel axis, and lower figures show the profiles perpendicular to the tunnel. Red points in the lower figure are the tunnel locations. (For interpretation of the references to color in this figure legend, the reader is referred to the web version of this article.)

maximum drawdown was predicted. The location of the drawdown exhibits a bottleneck behavior with a relatively small range of 18.6 m. The highest range on the high-influence zone in terms of the mean estimate is 185.4 m at the center of the tunnel line (3325.0 m distance) with 199.4 m drawdown from the natural water table, demonstrating the biggest impact on water table and the uncertainty induced by tunnel drainage.

4.2. Vulnerability assessment of terrestrial vegetation

The regional vulnerability analysis is present in a layered fashion by z_r as the percentage depth. For simplicity, we report depths of 10 %, 15 %, 25 %, 35 %, and 50 % starting from the soil surface ($z = 0$). Fig. 8 covers the vulnerability results simulated from mean drawdown estimates (μ_x); σ_x -based vulnerability maps are demonstrated in Fig. C1 (Appendix C). The drainage impact is interpreted using the vulnerability index (Section 2.2) and double vulnerability criteria (Section 2.1.4).

Fig. 8a-d show stress conditions at least in the top 25 % of the rooting depth ($Vin = 1$), occupying 53 % to 44 % of the total area by progressing through the deeper layer and rapidly changing to non-vulnerable conditions (Fig. 8e and f). Lighter colored areas correspond to shallow water zones with rivers and tributaries. While the shallow water area ($Vin < 0.05$) is expanding from the surface to the deeper rooting depth (4.3 % to 13.5 % in total area), the plants in locations with drainage-induced drawdown (Gray background contours in Fig. 8) remain vulnerable, particularly close to the tunnel axis. Despite the fact that the results indicate the first criteria ($h = h_w$ at z), double vulnerability criteria in the rooting zone were not satisfied in the region.

4.3. Uncertainty effect on vulnerability

The uncertainty effect in IVAF represents the impact of drainage-induced drawdown uncertainty on h , and thus the vulnerability. As a result, h reflects the hydraulic properties of both soil and rock environments. The vulnerability characteristics are not significantly different comparing the vulnerability maps for mean drawdown estimates (Fig. 8) and σ_x -based maps (Fig. C1). The former, on the other hand, indicates slightly more vulnerable zone ($Vin = 1$) by area (59 %, 58 %, 56 %, and 52 % from surface to 25 % of depth). Because the statistical dispersion caused by the drawdown predictions represented in σ_x -based maps, the point base differences between maps are depicted as vulnerability uncertainty in Fig. 9.

Fig. 9 compares the vulnerability uncertainty overlying depth-to-water table zones, where values indicate a probability of vulnerability. Both 1 and -1 are considered likely vulnerability conditions ($Vin = 1$). The red and gray scales demonstrate the vulnerability induced by tunnel drainage led by statistical dispersion from the mean prediction. The majority of drainage-induced vulnerability is concentrated in the zone where DWT is < 30 m. The zone outside of the outer gray contour (DWT > 30 m) exhibits minimal uncertainty, indicating that tunnel drainage has no influence. The central part of the tunnel, corresponding to the shallow water table area, and the areas close to the intersections shallow and deeper water table zones are both strongly influenced ($\leq 25\%$, Fig. 9a-d). In Fig. 9a-d, the impact on vulnerability greater than $| \pm 0.7 |$ occupies 3 %-4% of the total area.

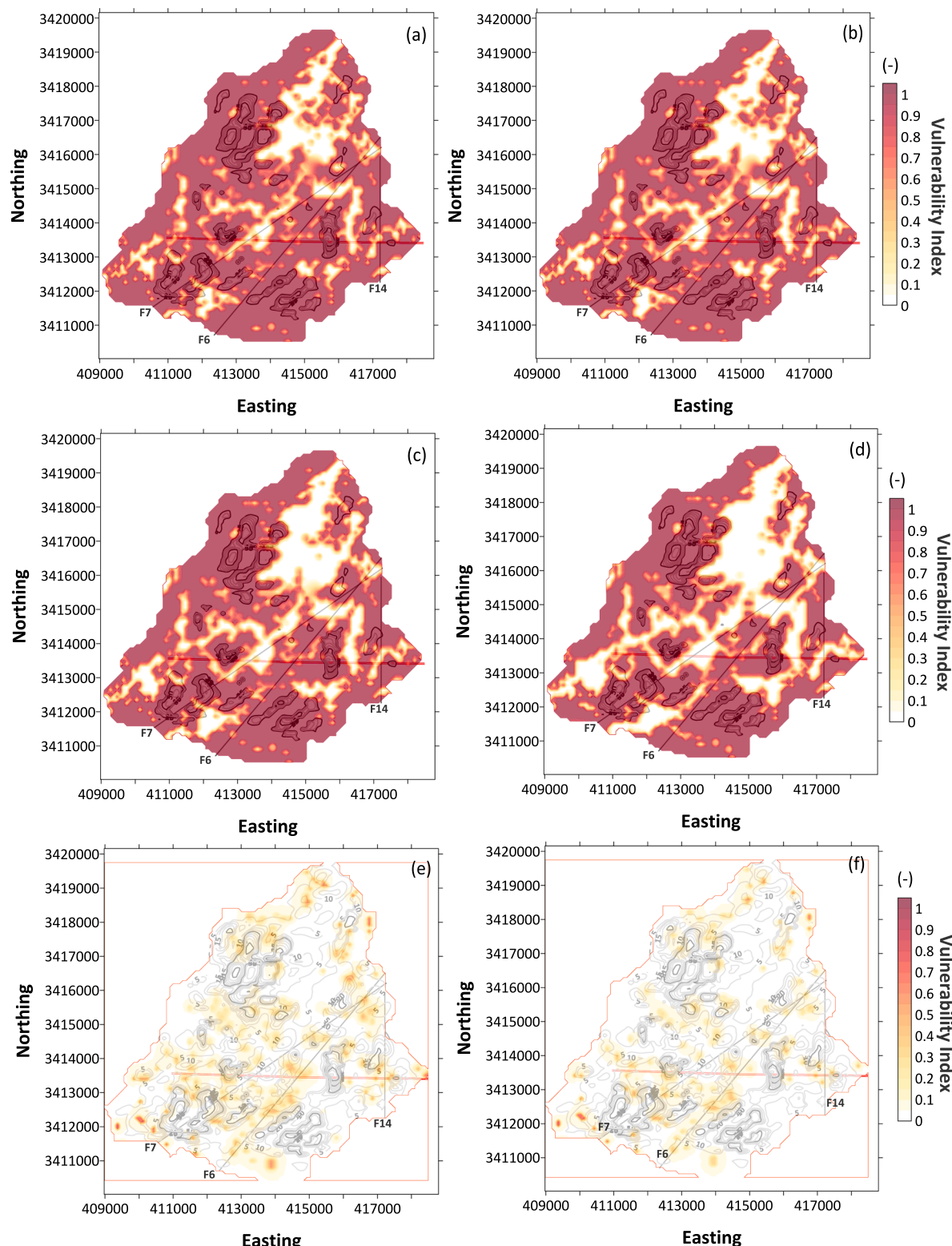


Fig. 8. Vulnerability maps based on relative rooting depth (z/δ) slices through the Mingtang tunnel area. The outcomes summarize vulnerability according to vulnerability concept as (a) surface level, (b) 10%, (c) 15%, (d) 25%, (e) 35%, and (f) 50% of rooting depth per point location. Gray contours represent predicted drawdown distribution from the stochastic model.

5. Discussion

5.1. Vulnerability assessment

In this assessment, the tunnel is simplified into a single circular

design with standard lining in the stochastic groundwater model with a daily drainage rate of 0.40 to 0.68 $\text{m}^3/\text{m-d}$, which falls within allowable rate for the ecological environment in the conventional engineering practice (Cheng et al., 2014; Fu et al., 2022). The total daily recharge exceeds the tunnel discharge rate when the hydraulic features of the

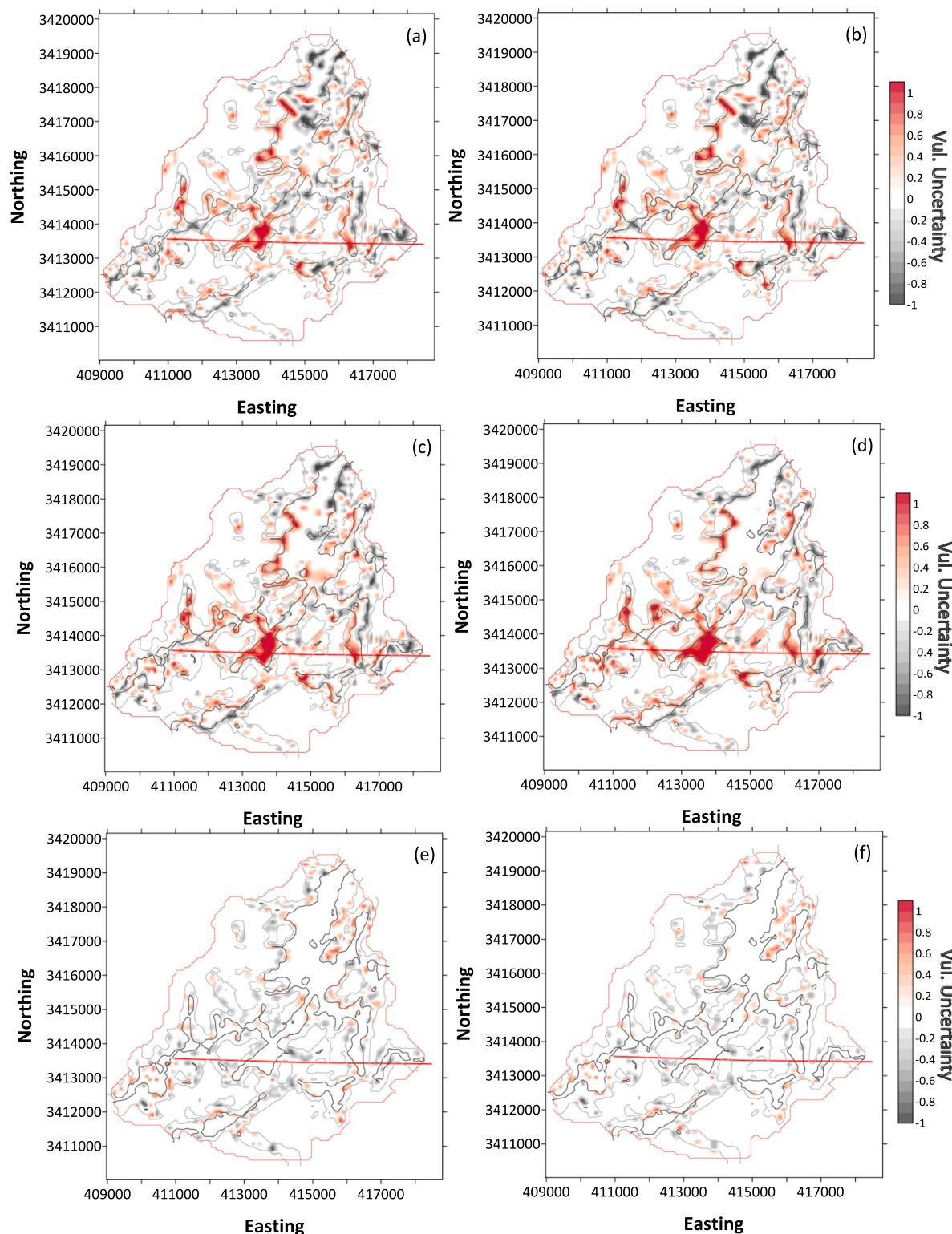


Fig. 9. Vulnerability uncertainty demonstrates an uncertainty effect on vulnerability assessment as relative rooting depth (z/δ) slices through the Mingtang area. The outcomes are on the range between [1, −1] as (a) surface level, (b) 10 %, (c) 15 %, (d) 25 %, (e) 35 %, and (f) 50 % of rooting depth per point location. The area outside of the outer gray color lines represents the deep water table zone (DWT > 30 m), and the inner black contour lines cover the shallower water table area (DWT < 5). The red line demonstrates the axis of the tunnel. (For interpretation of the references to color in this figure legend, the reader is referred to the web version of this article.)

rock settings and the estimated recharge rate seeping through the quaternary layer are taken into account (See areal rates in Table 1). As in the analytical methods (Cheng et al., 2019), rainfall replenishes the amount of water lost through tunnel drainage. The selected atmospheric data

demonstrate humid climate conditions throughout the year (2013), least likely leading the vegetation to be vulnerable (Gokdemir et al., 2021). Accordingly, the outcome of the framework suggests that vulnerability conditions for the study site are not met. However, in the presented set

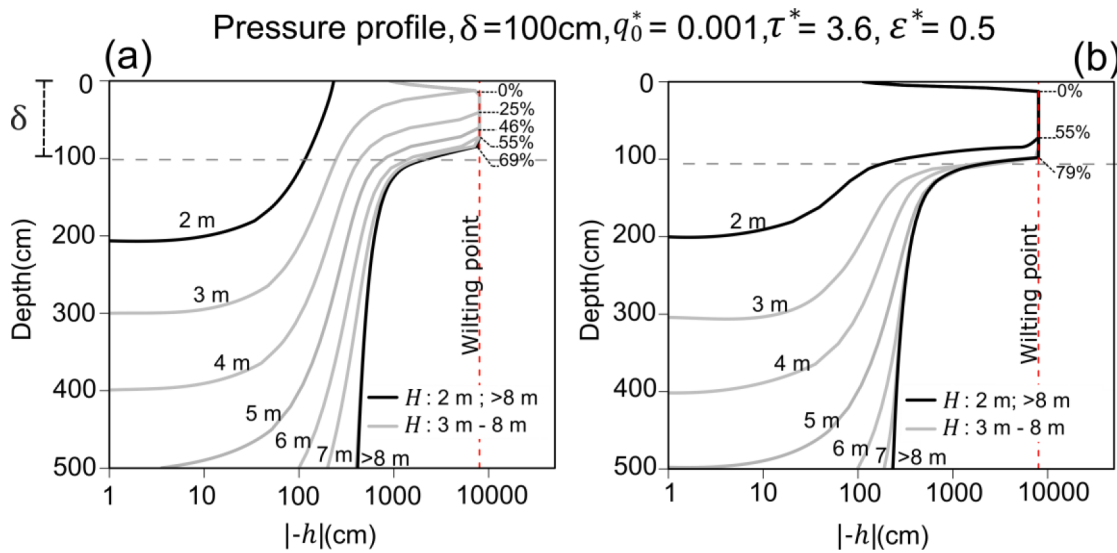


Fig. A1. Demonstration of dynamic wilting under changing water table, H in topsoil. Two numerical experiments are present with the same boundary conditions: (a) clay profile as low (3.6 cm d^{-1}) and (b) sandy loam as high (106 cm d^{-1}) saturated hydraulic conductivity cases. The rooting depth is assumed to be 100 cm with specified constant relative water flux q_0^* , transpiration τ^* , and evaporation ε^* .

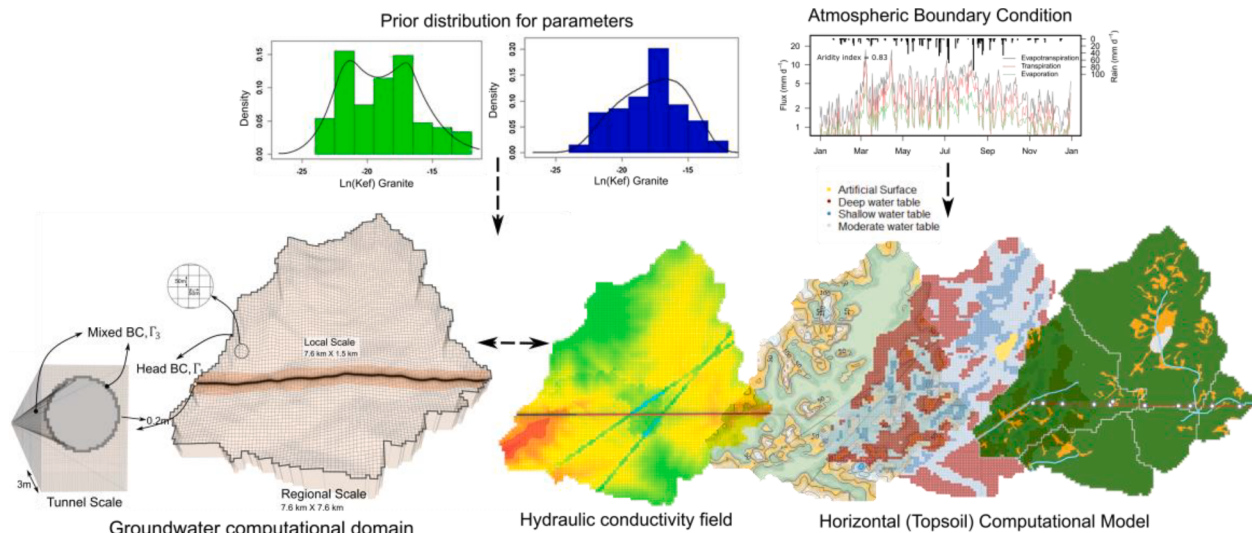


Fig. B1. The summary for integral vulnerability assessment method (IVAM) regarding numerical model scheme. Heterogeneous hydraulic conductivity fields are constructed for each groundwater simulation. Depth-to-water table is generated from probabilistic model with consecutive groundwater simulations. Accordingly, the segmentation of the depth-to-water table is shown in the horizontal computational model. Points on the domain except the yellow zone represent single soil profiles. (For interpretation of the references to color in this figure legend, the reader is referred to the web version of this article.)

of topsoil parameters, the spatial vulnerability analysis on catchment level reveals that 35 % of the upper rooting depth is under stress conditions (Fig. 8 and Fig. C1), indicating high V_{in} estimates. The tunnel-drainage impact assessment based on the DWT and related vulnerability index predictions shows that most of the catchment areas are influenced by atmospheric forcing - plant system interaction rather than tunnel drainage. The uncertainty analysis in Fig. 9 proves that the drainage-induced drawdown can impact the upper section of topsoil and lead to vulnerability when combined with shallow water table conditions. Even if terrestrial vegetation survives, forest growth dynamics and the fertility of cultivated land would suffer (Behzad et al., 2022).

5.2. Implementation of the framework

This study presents the integral vulnerability assessment framework (IVAF) as an application for tunnel drainage-induced vulnerability on

terrestrial vegetation for a specific deep tunnel project in a moderate-relief mountain region. From a tunneling standpoint, the framework is designed based on two important strategies; 1) a method that can be implemented with tunnel survey information without additional field measurement, and 2) providing ample results in a reasonable time without arduous calculations. In addition, by incorporating topography, rock, and soil types from the literature and tunnel feasibility reports, IVAF aims to reveal the catchment response to tunnel drainage.

The first strategy is met by introducing ex-situ input data from the literature for stochastic groundwater and topsoil models based on the similarity principle (Li et al., 2018) and linking simplifying assumptions, as shown in the integral vulnerability assessment method diagram (Fig. 3). Although we used a loosely integrated version of IVAF for this work, the data was transferred between numerical models simultaneously. The framework has been applied in an integrated environment written in R code (R-4.2.0 for windows), which links the Fortran-based

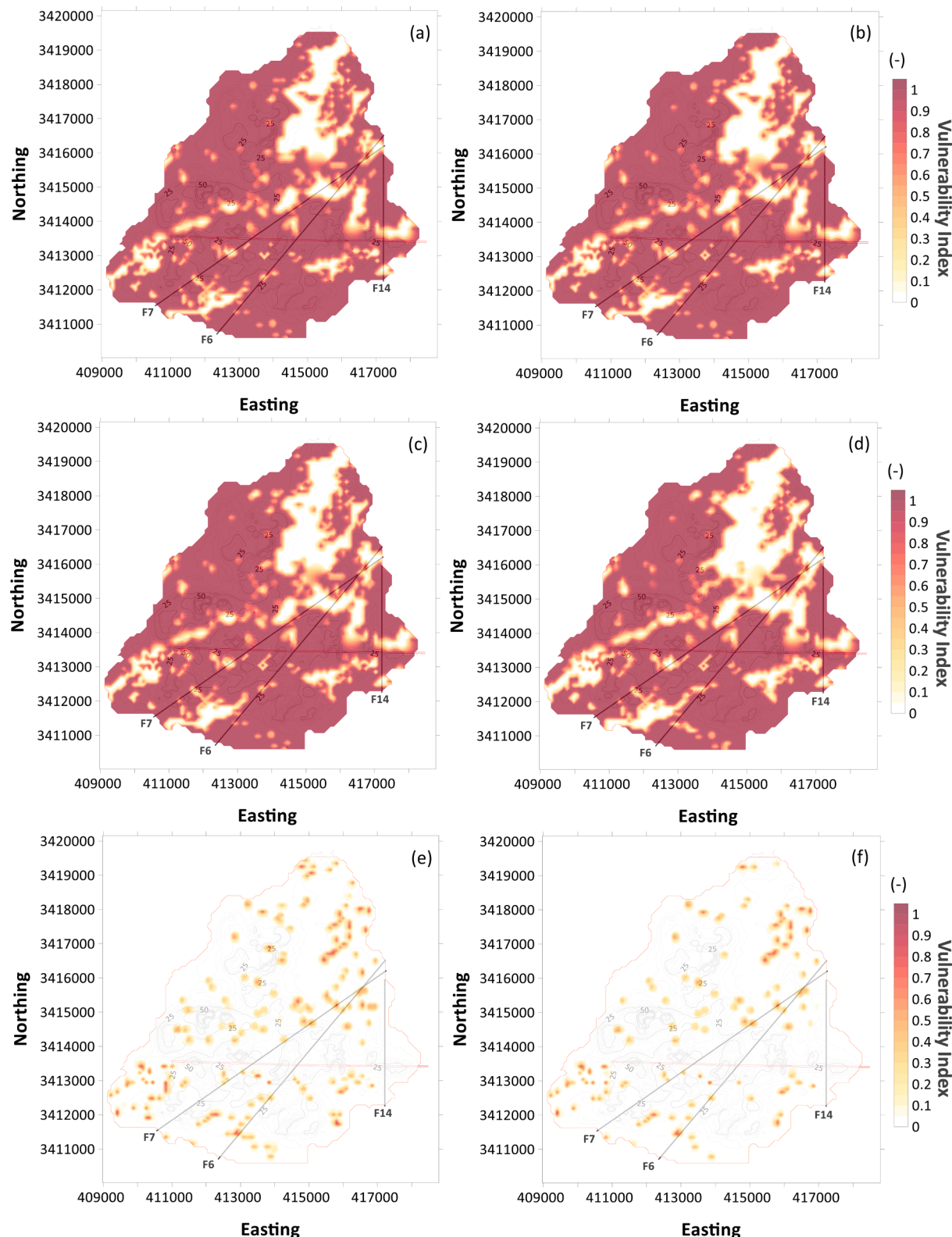


Fig. C1. Vulnerability maps, based on uncertainty predictions on relative rooting depth (z/δ) slices through Mingtang tunnel area. The outcomes summarize vulnerability according to vulnerability concept as (a) surface level, (b) 10%, (c) 15%, (d) 25%, (e) 35%, and (f) 50% of rooting depth per point location. Gray contours represent standard deviation distribution of drawdown per location from the stochastic model.

codes of Modflow and Hydrus-1D in a modular fashion. Even though the domains of the groundwater model (318,603 finite-difference cells) and topsoil (9,800 equidistant points) contain many computational units, requiring a good computing power, the entire process is completed in <6

h using Intel® Core™ i9-11950H 2.61Ghz machine with parallel computing.

In terms of usage, the framework outcomes have several layers, as one can gather the mean regional water table response (Fig. 6) or local

analysis based on a selected point or transect (Fig. 7) in the desired variation. We present regional vulnerability analysis for the multi-catchment region, but focusing on only cultivated land or any other designated zone and topsoil depth is possible. However, the uncertainty map is the final product of IVAF that is suggested to be used for the tunnel drainage-induced impact. The uncertainty maps in Fig. 9 also show the possibility of vulnerability in the highlighted areas caused solely by the tunnel drainage based on the statistical distance from the mean drawdown prediction. Therefore, uncertainty maps can also be called risk maps for terrestrial vegetation.

5.3. Limitations and potentials

There are two approaches to the drainage-induced water-table drawdown; analytical, numerical, or empirical methods (in-situ observations from tunneling sight) and those that emphasize the impact of drainage on environmental systems. In comparison to previous methods, IVAF connects these two approaches to evaluate the impact on terrestrial vegetation at a catchment level by including soil water hydrology. Because all of the IVAF components are individually complex systems, simplifications have been made.

The assessment method is intended to represent long-term effects using a steady-state solution, similar to the analytical methods commonly used in tunnel engineering. Therefore, dynamic factors such as seasonal water level changes on main river channels, small lakes, or reservoirs are excluded. Vertical water flow in the soil is the dominant factor, especially for the topsoil in mountainous areas. However, horizontal movement between soil columns or runoff would have a long-term impact on h . Another dynamic factor not considered in the framework is the vegetation growth and decay, which would cause plant system parameters (Eq. (9)) to change and affect τ_a estimations seasonally. In this study, a single year of static atmospheric forcing has been used, and the same atmospheric trend was maintained for the equilibrium conditions. The framework is adaptable enough to implement climatic trends, such as the implications of expected climate change scenarios (Chen and Sun, 2018), so the vulnerability risk can be extended with the climatic effect. The resolution of topsoil points is sufficient to represent land cover data for the simplified assessment, using a single-layered topsoil composition (Table 1) for the catchment. Regardless, the framework can be made more detailed by including remote sensing data for land cover and associated soil types, as well as advanced statistical techniques such as machine learning (Diaz-Gonzalez et al., 2022) to save from computation.

6. Conclusion and implications

This study presents the integral vulnerability assessment framework (IVAF), which provides a regional tunnel drainage impact assessment on terrestrial vegetation. The framework is applied using ex-situ data synthesis methods coupled with physical-based models. Accordingly, the stochastic groundwater model takes parameter values from a variety of data sources and solves regional groundwater flow based on parameter sets. Subsequently, the topsoil model runs over point depth-to-water

table predictions from the stochastic model. The IVAF offers the following novelties to tunnel engineers:

- Inclusion of the regional effect of tunnel drainage-induced drawdown with high- or moderate-relief topography.
- An evaluation based on variable land cover classifications (Chinese Fir, Tea), with the framework adaptable to include various vegetation system features with soil variability.
- Spatial risk assessment as vulnerability probability with drawdown uncertainty response.

Furthermore, specific to the case study, IVAF outcomes provide two significant insights for the tunnel drainage impact assessment:

- Long-term drawdown exhibits irregular and variable behavior, causing drawdown all over the multi-catchment area (with an average of 10.73 m), reflecting topography and groundwater flow direction.
- Even though there is sufficient rainfall in the catchment area, drainage-induced drawdown may cause stress conditions in the rooting zone of terrestrial vegetation, especially as a result of the transition from shallow to deep drawdown zones.

CRediT authorship contribution statement

Cagri Gokdemir: Writing – original draft, Conceptualization, Methodology, Software, Validation, Formal analysis, Data curation, Visualization, Funding acquisition. **Yi Rui:** Writing – review & editing. **Yoram Rubin:** Conceptualization, Methodology, Writing – review & editing. **Xiaojun Li:** Supervision, Writing – review & editing, Resources, Project administration, Funding acquisition.

Declaration of Competing Interest

The authors declare that they have no known competing financial interests or personal relationships that could have appeared to influence the work reported in this paper.

Data availability

We have included related scripts and data by the request of 2nd Reviewer.

Acknowledgements

The research was conducted with support from the Natural Science Foundation of China (Grant No. 41877246), and Sponsored by Anhui Transportation Holding Group Co., Ltd. (JKKJ-2020-10) and the Program of Shanghai Academic/Technology Research Leader (22XD1403400). We thank Prof. Jirka Šimůnek for sharing the soil profile discretization algorithm in the Hydrus-1D graphical editor with us.

Appendix A

This appendix contains numerical experiment results for vulnerability analysis that show dynamic root-zone wilting behavior as a function of the groundwater table. Fig. A1 demonstrates the non-linear alterations on h profiles caused by changing water table conditions.

Numerical experiments have been conducted to investigate the relationship between the dynamic wilting and groundwater table conditions in clay and sandy loam soil textures. To have comparable responses of h for different soil textures, specific soil profiles are set based on relative fluxes q_0^* ($= q_0/K_s$), τ^* ($= \tau/q_0$), and ε^* ($= \varepsilon/q_0$). The numerical experiments reveal that the vulnerability conditions have a non-linear relationship with the water table located in a one-dimensional space. In both cases, in Fig. A1, a water table of >8 m has no effect on the rooting zone, and vulnerability conditions are reached on a 5 m water table in clay soil (Fig. A1a) and 2 m in sandy loam soil (Fig. A1b).

Appendix B

The IVAF includes a coupled numerical model scheme that exchanges data between topsoil (1-D) and groundwater (3-D) models. The groundwater model used to solve water flow is included in a probabilistic formula as a forward model rather than being directly coupled with topsoil model. The drawdown estimations are transferred into the topsoil layer as the bottom boundary condition. Consequently, the stochastic groundwater model can also be referred to as stochastic modelling of groundwater drawdown using the Bayesian technique. As a result, the methodological basis and integration have been outlined in this section.

B.1. Data preparation

IVAF framework aims to provide predictions to tunneling professionals during the tunnel design process before construction. Therefore, the data strategy is adopted based on poorly sampled or no-data site conditions. As shown in Fig. 3, data is collected under six classifications, where daily meteorological data, soil physics, and plant physiology are included topsoil model (See Table 1). In contrast, topography and hydrology, hydrogeology, and tunnel data are represented in the groundwater model. The parameter values from the data included in IVAF are based on the theories explained in Section 2.1.

The meteorological data is collected from local authorities and weather station readings. Partitioning of parameters is calculated based on the model explained in Section 2.1.1 coupled with plant information. Accordingly, plant physiology and soil physics are formed in a compilation of geographical information system (GIS) data, site campaigns, and literature. Similarly, topography and hydrology data are mostly created from GIS information.

Apart from the other data types, hydrogeological data is required additional treatment for fault zone and corresponding rock types. Due to a lack of hydrogeological data, the parameter space for the groundwater model is constructed using a probabilistic approach. Therefore, prior distributions (See density distributions in Fig. B1) prepared separately for granite, gneiss, and corresponding fault zones have been prepared from the ex-situ data sets based on the site similarity principle. Prior distributions are used in Eq. (13) as $P(H_j|e_k)$. The sites have been chosen based on similarities in geological structure, fracture condition, tectonic condition, sampling depth, and sampling method (Li et al., 2018).

B.2. Groundwater model

As mentioned in Section 2.2.1, the groundwater model in IVAF estimates drawdown predictions for a given set of parameter values (Table 1). To represent both complex mountainous topography and tunnel details, the model domain is generated using telescopic mesh refinement (Leake and Claar, 1999) with grid sizes ranging from 0.2 to 373.5 m (Fig. B1). To represent three-dimensional rock-type segmentation, the rock type distribution is obtained using conditional sequential indicator simulation (Bastante et al., 2008) on borehole data.

As the key parameter for groundwater flow, effective hydraulic conductivities estimated from ex-situ data is implemented in the domain considering exponential decrease as a function of depth (Bense et al., 2013). The rate of the decrease is derived in the form of regression model as follows;

$$\ln(K_s) = a + b e^{-cx}. \quad (\text{B1})$$

where a, b, and c are regression coefficients and x is the rock matrix depth. This model was implemented for gneiss, granite and fault zones (Gokdemir et al., 2022). The estimations steps are listed in Li et al. (2018). Sets of hydraulic conductivity distributions are generated by integrating regression model over the groundwater domain (Fig. B1).

Simulations have been run successively; each simulation result is a collection of drawdown values for a given parameter combination within defined boundary conditions (See section 2.2.1). For each simulation, tunnel inflow rates were predicted due to the mixed boundary condition imposed over the tunnel line. The numerical solution sets are selected based on tunnel inflow error intervals (e_k).

B.3. Implementation of topsoil model

The topsoil domain is represented by the vertical computational domain, and the region illustrated in Fig. B1 is represented by the horizontal computational domain. For each place, the designated boundary requirements outlined in Section 2.2.2 are mandated. Based on the land cover, different parameter sets and boundary values are applied to each plant species. The points' segmentation is arranged based in DWT values, where $DWT > 30$ m, $1m < DWT \leq 30$ m, and $DWT \leq 1$ m have denoted as deep, moderate, and shallow water table zones. Gradient-type boundary conditions apply to the deep water table zone, while the rest are subjected to head boundary conditions.

Appendix C

In the following figure, vulnerability maps based on drawdown uncertainty are presented. The uncertainty is represented as standard deviation per point location from the stochastic groundwater model.

References

- Allen, R.G., Pereira, L.S., Raes, D., Smith, M., 1998. Crop evapotranspiration-Guidelines for computing crop water requirements-FAO Irrigation and drainage paper 56. Fa, Rome 300, D05109.
- Bastante, F.G., Ordóñez, C., Taboada, J., Matías, J.M., 2008. Comparison of indicator kriging, conditional indicator simulation and multiple-point statistics used to model slate deposits. Eng. Geol. 98, 50–59. <https://doi.org/10.1016/j.enggeo.2008.01.006>.
- Behzad, H.M., Jiang, Y., Arif, M., Wu, C., He, Q., Zhao, H., Lv, T., 2022. Tunneling-induced groundwater depletion limits long-term growth dynamics of forest trees. Sci. Total Environ. 811, 152375 <https://doi.org/10.1016/j.scitotenv.2021.152375>.
- Bense, V.F., Gleeson, T., Loveless, S.E., Bour, O., Scibek, J., 2013. Fault zone hydrogeology. Earth-Sci. Rev. 127, 171–192.
- Butscher, C., 2012. Steady-state groundwater inflow into a circular tunnel. Tunn. Undergr. Sp. Technol. 32, 158–167. <https://doi.org/10.1016/j.tust.2012.06.007>.
- Carsel, R.F., Parrish, R.S., 1988. Developing joint probability distributions of soil water retention characteristics. Water Resour. Res. 24, 755–769. <https://doi.org/10.1029/WR024i005p00755>.
- Chen, J., Cao, X., Peng, S., Ren, H., 2017. Analysis and Applications of GlobeLand30 : A Review 1–16. <https://doi.org/10.3390/ijgi6080230>.
- Chen, H., Sun, J., 2018. Projected changes in climate extremes in China in a 1.5 °C warmer world. Int. J. Climatol. 38, 3607–3617. <https://doi.org/10.1002/joc.5521>.
- Chen, G.S., Yang, Z.J., Gao, R., Xie, J.S., Guo, J.F., Huang, Z.Q., Yang, Y.S., 2013. Carbon storage in a chronosequence of Chinese fir plantations in southern China. For. Ecol. Manage. 300, 68–76. <https://doi.org/10.1016/j.foreco.2012.07.046>.
- Chen, J., Zhu, H., Li, X., 2016. Automatic extraction of discontinuity orientation from rock mass surface 3D point cloud. Comput. Geosci. 95, 18–31. <https://doi.org/10.1016/j.cageo.2016.06.015>.
- Cheng, P., Zhao, L., Luo, Z., Li, L., Li, Q., Deng, X., Peng, W., 2019. Analytical solution for the limiting drainage of a mountain tunnel based on area-well theory. Tunn. Undergr. Sp. Technol. 84, 22–30. <https://doi.org/10.1016/j.tust.2018.10.014>.

- Cheng, P., Zhao, L., Li, L., Zou, J., Luo, W., 2014. Limiting drainage criterion for groundflow of mountain tunnel. *J. Cent. South Univ.* 21, 4660–4668. <https://doi.org/10.1007/s11771-014-2474-6>.
- Chu, Z., Wu, Z., Liu, B., Wu, K., Shi, X., Liu, Q., 2022. Mechanical response of inclined TBM tunnel due to drainage settlement of deep sandstone aquifer. *Tunn. Undergr. Sp. Technol.* 122, 104393. <https://doi.org/10.1016/j.tust.2022.104393>.
- Condon, L.E., Maxwell, R.M., 2015. Evaluating the relationship between topography and groundwater using outputs from a continental-scale integrated hydrology model. *Water Resour. Res.* 51, 6602–6621. <https://doi.org/10.1002/2014WR016774>.
- Cooper, D.J., Sanderson, J.S., Stannard, D.I., Groeneweld, D.P., 2006. Effects of long-term water table drawdown on evapotranspiration and vegetation in an arid region phreatophyte community. *J. Hydrol.* 325, 21–34. <https://doi.org/10.1016/j.jhydrol.2005.09.035>.
- de Jong van Lier, Q., Metselaar, K., van Dam, J.C., 2006. Root water extraction and limiting soil hydraulic conditions estimated by numerical simulation. *Vadose Z.* 6, 527. <https://doi.org/10.2136/vzj2006.0056>.
- Diaz-Gonzalez, F.A., Vuelvas, J., Correa, C.A., Vallejo, V.E., Patino, D., 2022. Machine learning and remote sensing techniques applied to estimate soil indicators – review. *Ecol. Ind.* 135, 108517. <https://doi.org/10.1016/j.ecolin.2021.108517>.
- dos Santos, M.A., de Jong van Lier, Q., van Dam, J.C., Freire Bezerra, A.H., 2017. Benchmarking test of empirical root water uptake models. *Hydrol. Earth Syst. Sci.* 21 (1), 473–493.
- Duan, M., Xie, J., Mao, X., 2019. Modeling water and heat transfer in soil-plant-atmosphere continuum applied to maize growth under plastic film mulching. *Front. Agr. Sci. Eng.* 6 (2), 144.
- El Tani, M., 2003. Circular tunnel in a semi-infinite aquifer. *Tunn. Undergr. Sp. Technol.* 18, 49–55. [https://doi.org/10.1016/S0886-7798\(02\)00102-5](https://doi.org/10.1016/S0886-7798(02)00102-5).
- Fahadian, H., Nikvar-Hassani, A., 2019. Water flow into tunnels in discontinuous rock: a short critical review of the analytical solution of the art. *Bull. Eng. Geol. Environ.* 78, 3833–3849. <https://doi.org/10.1007/s10064-018-1348-9>.
- Farooq, T.H., Yan, W., Chen, X., Shakoor, A., Rashid, M.H.U., Gilani, M.M., He, Z., Wu, P., 2020. Dynamics of canopy development of Cunninghamia lanceolata mid-age plantation in relation to foliar nitrogen and soil quality influenced by stand density. *Glob. Ecol. Conserv.* 24, e01209.
- Feddes, R.A., Bresler, E., Neuman, S.P., 1974. Field test of a modified numerical model for water uptake by root systems. *Water Resour. Res.* 10, 1199–1206. <https://doi.org/10.1029/WR010i006p01199>.
- Feddes, R.A., Kowalik, P.J., Zaradny, H., 1978. *Simulation of Field Water Use and Crop Yield*. A Halsted Press book, Wiley.
- Feddes, R.A., Hoff, H., Bruen, M., Dawson, T., de Rosnay, P., Dirmeyer, P., Jackson, R.B., Kabat, P., Kleidon, A., Lilly, A., Pitman, A.J., 2001. Modeling root water uptake in hydrological and climate models. *Bull. Am. Meteorol. Soc.* 82 (12), 2797–2809. [https://doi.org/10.1175/1520-0477\(2001\)082<2797:MRWUH>2.3.CO;2](https://doi.org/10.1175/1520-0477(2001)082<2797:MRWUH>2.3.CO;2).
- Fernandez, G., Moon, J., 2010. Excavation-induced hydraulic conductivity reduction around a tunnel – Part 1: Guideline for estimate of ground water inflow rate. *Tunn. Undergr. Sp. Technol.* 25, 560–566. <https://doi.org/10.1016/j.tust.2010.03.006>.
- Fu, H., An, P., Cheng, G., Wen, S., Li, J., 2022. Calculation of the allowable drainage of parallel tunnels based on ecological environment protection. *KSCE J. Civ. Eng.* 26, 2420–2427. <https://doi.org/10.1007/s12205-022-0401-1>.
- Gisbert, J., Vallejos, A., Gonzalez, A., Pulido-Bosch, A., 2009. Environmental and hydrogeological problems in karstic terrains crossed by tunnels: a case study. *Environ. Geol.* 58, 347–357. <https://doi.org/10.1007/s00254-008-1609-1>.
- Gleeson, T., Manning, A.H., 2008. Regional groundwater flow in mountainous terrain: three-dimensional simulations of topographic and hydrogeologic controls. *Water Resour. Res.* 44. <https://doi.org/10.1029/2008WR006848>.
- Gokdemir, C., Rubin, Y., Li, X., Li, Y., Xu, H., 2019. Vulnerability analysis method of vegetation due to groundwater table drawdown induced by tunnel drainage. *Adv. Water Resour.* 133, 103406.
- Gokdemir, C., Rubin, Y., Li, X., Xu, H., 2021. A vulnerability assessment method to evaluate the impact of tunnel drainage on terrestrial vegetation under various atmospheric and climatic conditions. *Adv. Water Resour.* 147, 103796.
- Gokdemir, C., Li, Y., Rubin, Y., Li, X., 2022. Stochastic modeling of groundwater drawdown response induced by tunnel drainage. *Eng. Geol.* 297, 106529.
- Gower, S.T., Kucharik, C.J., Norman, J.M., 1999. Direct and indirect estimation of leaf area index, FAPAR, and net primary production of terrestrial ecosystems. *Remote Sens. Environ.* 70, 29–51. [https://doi.org/10.1016/S0034-4257\(99\)00056-5](https://doi.org/10.1016/S0034-4257(99)00056-5).
- Grinevskii, S.O., 2014. The effect of topography on the formation of groundwater recharge. *Mosc. Univ. Geol. Bull.* 69, 47–52. <https://doi.org/10.3103/S0145875214010025>.
- Guo, Y., Qin, D., Li, L., Sun, J., Li, F., Huang, J., 2019. A Complicated Karst Spring System Identified by Karst Springs Using Water Level, Hydrogeochemical, and Isotopic Data in Jinan, China. *Water.* <https://doi.org/10.3390/w11050947>.
- Harbaugh, Arlen, W., Harbaugh, A.W., 2005. MODFLOW-2005 : the U.S. Geological Survey modular ground-water model—the ground-water flow process, Techniques and Methods. <https://doi.org/10.3133/tm6A16>.
- Hosty, M., Mulqueen, J., 1996. Soil moisture and groundwater drawdown in a dry grassland soil. *Irish J. Agric. Food Res.* 35, 17–24.
- Jin, X., Wan, L., Zhang, Y., Xue, Z., Yin, Y., 2007. A study of the relationship between vegetation growth and groundwater in the yinchuan plain. *Earth Sci. Front.* 14, 197–203. [https://doi.org/10.1016/S1872-5791\(07\)60026-8](https://doi.org/10.1016/S1872-5791(07)60026-8).
- Jukaine, Laine, J., Vasander, H., Laiho, R., 1995. Long-Term Effects of Water Level Drawdown on the Vegetation of Drained Pine Mires in Southern Finland. *J. Appl. Ecol.* 32, 785–802. <https://doi.org/10.2307/2404818>.
- Kolymbas, D., Wagner, P., 2007. Groundwater ingress to tunnels – the exact analytical solution. *Tunn. Undergr. Sp. Technol.* 22, 23–27. <https://doi.org/10.1016/j.tust.2006.02.001>.
- Leake, S.A., Claar, D.V., 1999. Procedures and computer programs for telescopic mesh refinement using MODFLOW. Open-File Report. <https://doi.org/10.3133/ofr99238>.
- Li, X., Chen, J., Zhu, H., 2016. A new method for automated discontinuity trace mapping on rock mass 3D surface model. *Comput. Geosci.* 89, 118–131. <https://doi.org/10.1016/j.cageo.2015.12.010>.
- Li, X., Li, Y., Chang, C.F., Tan, B., Chen, Z., Sege, J., Wang, C., Rubin, Y., 2018. Stochastic, goal-oriented rapid impact modeling of uncertainty and environmental impacts in poorly-sampled sites using ex-situ priors. *Adv. Water Resour.* 111, 174–191. <https://doi.org/10.1016/j.advwatres.2017.11.008>.
- Likos, W.J., Lu, N., Godt, J.W., 2014. Hysteresis and uncertainty in soil water-retention curve parameters. *J. Geotech. Geoenvironmental Eng.* 140, 04013050. <https://doi.org/10.1016/j.gat.2014.03.001>.
- Liu, J., Liu, D., Song, K., 2015. Evaluation of the influence caused by tunnel construction on groundwater environment: a case study of tongluoshan tunnel. *China. Adv. Mater. Sci. Eng.* 149265.
- Liu, J., Shen, L., Wang, Z., Duan, S., Wu, W., Peng, X., Wu, C., Jiang, Y., 2019. Response of plants water uptake patterns to tunnels excavation based on stable isotopes in a karst trough valley. *J. Hydrol.* 571, 485–493. <https://doi.org/10.1016/j.jhydrol.2019.01.073>.
- Monteith, J.L., 1981. Evaporation and surface temperature. *Q. J. R. Meteorol. Soc.* 107, 1–27. <https://doi.org/10.1002/qj.49710745102>.
- Monteith, J.L., Unsworth, M.H.B.T.-P. of E.P. (Fourth E. (Eds.), 2013. *Principles of Environmental Physics*. Academic Press, Boston, p. iii. <https://doi.org/10.1016/B978-0-12-386910-4.00019-6>.
- Niranjan, K.S., Viswanath, S., 2008. Root characteristics of tea (*Camellia sinensis* (L.) O. Kuntze) and silver oak (*Grevillea robusta* (A. Cunn)) in a mixed tea plantation at Munnar, Kerala. *J. Trop. Agric.* 25–31.
- Norman, J.M., Anderson, M.C., 2005. In: *Encyclopedia of Soils in the Environment*. Elsevier, pp. 513–521.
- Rajapakse, R.M.S.S., Tripathi, N.K., Honda, K., 2002. Spectral characterization and LAI modelling for the tea (*Camellia sinensis* (L.) O. Kuntze) canopy. *Int. J. Remote Sens.* 23, 3569–3577. <https://doi.org/10.1080/01431160110114583>.
- Rasouli Maleki, M., 2018. Groundwater Seepage Rate (GSR); a new method for prediction of groundwater inflow into jointed rock tunnels. *Tunn. Undergr. Sp. Technol.* 71, 505–517. <https://doi.org/10.1016/j.tust.2017.10.006>.
- Ribacchi, R., Graziani, A., Boldini, D., 2002. Previsione degli afflussi d'acqua in galleria ed influenza sull'ambiente. In: Barla, G., Barla, M. (Eds.), *MEccanica E IngEgnEria DEIE Rocce. MIR*, Torino, pp. 143–199.
- Rubin, Y., Or, D., 1993. Stochastic modeling of unsaturated flow in heterogeneous soils with water uptake by plant roots: the parallel columns model. *Water Resour. Res.* 29, 619–631. <https://doi.org/10.1029/92WR02292>.
- Schaller, M.F., Fan, Y., 2009. River basins as groundwater exporters and importers: implications for water cycle and climate modeling. *J. Geophys. Res. Atmos.* 114. <https://doi.org/10.1029/2008JD010636>.
- Scheidler, S., Huggenberger, P., Butscher, C., Dreßmann, H., 2019. Tools to simulate changes in hydraulic flow systems in complex geologic settings affected by tunnel excavation. *Bull. Eng. Geol. Environ.* 78 (2), 969–980. <https://doi.org/10.1007/s10064-017-1113-5>.
- Šimůnek, J., M. Šejna, A., Saito, H., Sakai, M., Genuchten, M.T. Van, Šejna, M., Saito, H., Sakai, M., van Genuchten, M.T., 2013. The HYDRUS-1D Software Package for Simulating the Movement of Water, Heat, and Multiple Solutes in Variably Saturated Media, Version 4.17, HYDRUS Software Series 3. Riverside, California, USA.
- Su, K., Zhou, Y., Wu, H., Shi, C., Zhou, L., 2017. An analytical method for groundwater inflow into a drained circular tunnel. *Groundwater* 55, 712–721. <https://doi.org/10.1111/gwat.12513>.
- Sweetenham, M.G., Maxwell, R.M., Santi, P.M., 2017. Assessing the timing and magnitude of precipitation-induced seepage into tunnels bored through fractured rock. *Tunn. Undergr. Sp. Technol.* 65, 62–75. <https://doi.org/10.1016/j.tust.2017.02.003>.
- van Genuchten, M.T., 1980. A closed-form equation for predicting the hydraulic conductivity of unsaturated soils1. *Soil Sci. Soc. Am. J.* 44 (5), 892–898.
- Vincenzi, V., Gargini, A., Goldscheider, N., 2009. Using tracer tests and hydrological observations to evaluate effects of tunnel drainage on groundwater and surface waters in the Northern Apennines (Italy). *Hydrogeol J* 17, 135–150. <https://doi.org/10.1007/s10040-008-0371-5>.
- Vincenzi, V., Gargini, A., Goldscheider, N., Piccinini, L., 2014. Differential hydrogeological effects of draining tunnels through the northern Apennines. *Italy. Rock Mech. Rock Eng.* 47, 947–965. <https://doi.org/10.1007/s00603-013-0378-7>.
- Wan, L., Cao, W., Hu, F., Jin, X., Chen, J., Gong, B., 2005. *Ecological hydrogeology*, 1st ed. Geological Publishing House, Beijing.
- Wang, J., Jin, M., Lu, G., Zhang, D., Kang, F., Jia, B., 2016. Investigation of discharge-area groundwaters for recharge source characterization on different scales: the case of Jinan in northern China. *Hydrogeol J* 24 (7), 1723–1737. <https://doi.org/10.1007/s10040-016-1428-5>.
- Yeh, P.-J.-F., Eltahir, E.A.B., 2005. Representation of water table dynamics in a land surface scheme. Part I: Model Development. *J. Clim.* 18, 1861–1880. <https://doi.org/10.1175/JCLI3301.1>.

- Yoo, C., Lee, Y., Kim, S.-H., Kim, H.-T., 2012. Tunnelling-induced ground settlements in a groundwater drawdown environment – a case history. *Tunn. Undergr. Sp. Technol.* 29, 69–77. <https://doi.org/10.1016/j.tust.2012.01.002>.
- Zangerl, C., Eberhardt, E., Loew, S., 2003. Ground settlements above tunnels in fractured crystalline rock: numerical analysis of coupled hydromechanical mechanisms. *Hydrogeol. J.* 11, 162–173. <https://doi.org/10.1007/s10040-002-0234-4>.
- Zhao, Y., Li, P., Tian, S., 2013. Prevention and treatment technologies of railway tunnel water inrush and mud gushing in China. *J. Rock Mech. Geotech. Eng.* 5, 468–477. <https://doi.org/10.1016/j.jrmge.2013.07.009>.